METTL5 Blockade Enhances Anti-Tumor Immune Response via Inducing Neoantigen Generation

Yangyi Zhang[1, #], Xiaoyan Shi[1, #], Yuci Wang[1, 2, #], Ruiqi Wang[1], Yanlan Cao[1], Hao Chen[1, *]

[1]Department of Human Cell Biology and Genetics, SUSTech Homeostatic Medicine Institute, School of Medicine, Southern University of Science and Technology, Shenzhen 518055, Guangdong, China

[2]Peking university, Beijing, 100000, China

[#]These authors contributed equally to this work.

*Corresponding author. chenh7@sustech.edu.cn (H.C.).

ABSTRACT

Tumor neoantigens play a pivotal role in immunotherapy through eliciting tumor-specific immune responses. However, their clinical application is limited by the restricted repertoire of naturally occurring neoantigens, which undergoes continuous immune editing within the tumor microenvironment. To address this critical challenge, we explored translational regulation as a reversible and safer strategy to augment neoantigen production. Through systematic analysis of translational regulatory factors associated with immunotherapy response, we identified METTL5 as a key modulator of anti-tumor immunity. METTL5 depletion in syngeneic tumor models demonstrated significant enhancement of endogenous anti-tumor immunity across distinct MHC-I haplotypes, with synergistic effects observed when combined with immune checkpoint blockade. Based on evolutionary conservation of ribosomal decoding center modifications and established mechanisms from prokaryotic studies, we propose that METTL5-mediated m^6A modification at the small ribosomal subunit decoding center may contribute to translational fidelity regulation. Mechanistically, integrated MHC-I immunoprecipitation-mass spectrometry and ribosome profiling revealed the identification of non-canonical peptides, including those derived from novel unannotated open reading frames (nuORFs), which provide previously absent neoantigen sources for tumor cells. T-cell receptor sequencing further demonstrated significantly enhanced clonal diversity and tumor-specific reactivity of infiltrating T cells in METTL5-deficient tumors. Therapeutic vaccination strategies targeting METTL5-deficiency-induced neoantigens, including both peptide-based and mRNA vaccines, exhibited partial anti-tumor efficacy in murine tumor models. This study establishes METTL5 as a critical translational regulator that restricts neoantigen diversity and proposes a novel combinatorial strategy to enhance immunotherapy through translational control.

INTRODUCTION

The complexity of cancer therapy originates from the high heterogeneity of tumors, dynamic immune escape mechanisms, and the multi-faceted challenges posed by the immunosuppressive tumor microenvironment[1-8]. Conventional therapies (e.g., chemotherapy and radiotherapy) often cause severe toxic side effects with limited therapeutic efficacy, whereas immunotherapy, despite its advantages of low toxicity and durable responses, remains constrained by low response rates and the development of acquired resistance. [3-5,9-16]. Strategies targeting universal or single antigens are particularly vulnerable to failure due to antigen loss or exhaustion, and they fail to address tumor heterogeneity while introducing risks of immune-related adverse events (irAEs)[17-20].

A promising solution lies in the identification of tumor-specific mutations to generate neoantigens, which can activate polyclonal T-cell responses, overcome immune tolerance, and avoid off-target toxicity[21-28]. This "dynamic targeting" approach offers a means to address heterogeneity and drug resistance[4,5,29,30]. Neoantigens, derived from short peptides (8–25 amino acids) resulting from errors in gene expression regulation, are presented on tumor cell surfaces via human leukocyte antigen (HLA) molecules, enabling T-cell recognition[31-34]. Unlike self-antigens, neoantigens are not subject to central tolerance mechanisms and exhibit robust immunogenicity, making them ideal targets for immunotherapy[21,22,25,27,35-37].

Tumor mutational burden (TMB) has been proposed as a key biomarker in cancer immunotherapy, particularly for PD-1/PD-L1 inhibitors[38-42]. Moreover, TMB as a potential biomarker, exhibits cancer-type-dependent predictive value in PD-1/PD-L1 inhibitor treatments (e.g., non-small cell lung cancer and melanoma)[43,44]. Importantly, TMB represents only one pathway contributing to neoantigen generation. Certain tumor mutations enhance the quality and quantity of functional neoantigens, such as those

targeting highly immunogenic mutations like KRAS G12D, IDH1 R132H, and TP53 [45-48]. These neoantigen vaccines have demonstrated the ability to activate T-cell responses and penetrate the blood-brain barrier in solid tumors such as pancreatic cancer and glioma. Furthermore, the combination of personalized vaccines (e.g., NeoVax) with immune checkpoint inhibitors has advanced clinical exploration in precision immunotherapy, suggesting that the quality of neoantigens generated by tumor mutations may guide therapeutic efficacy[49].

However, clinical application of neoantigen-targeted therapies faces multiple challenges. First, most antigens arising from tumor mutations are of low quality (e.g., synonymous mutations or cryptic epitopes), exhibiting insufficient immunogenicity[50-54]. Second, certain mutated peptides share high sequence homology with self-proteins, leading to weakened anti-tumor immune responses due to central tolerance (thymic selection) or peripheral tolerance (T cell exhaustion) mechanisms[16,55]. More critically, the process of immune editing within the tumor microenvironment continuously eliminates highly immunogenic epitopes, leaving residual antigen pools dominated by low-affinity variants that further impair T cell activation efficiency[52,56]. To overcome these limitations, current intervention strategies-such as CRISPR/Cas9-induced mutations or DNA-damaging agents to enhance neoantigen load—can transiently expand neoantigen numbers[5,57,58]. However, their irreversible genomic modifications risk exacerbating tumor heterogeneity or causing normal tissue toxicity, significantly hindering clinical translation[59,60].

Compared to genomic interventions, translational regulation offers unique advantages for neoantigen development: First, the reversibility of translation allows dynamic control of ribosomal function (e.g., modulating methylation levels at the decoding center) to flexibly adjust translational error rates, avoiding permanent genomic alterations caused by CRISPR or DNA-damaging agents[61-67]. Second, as translational

regulation does not directly interfere with DNA sequences, its risks of carcinogenesis and off-target effects are markedly reduced, enhancing clinical safety[63]. Critically, peptide variants generated through translational misreading exhibit high spatiotemporal heterogeneity[62,66]. These transiently existing non-self-epitopes can effectively evade immune editing pressures, breaking immune tolerance induced by fixed mutation-derived epitopes[67]. Consequently, epigenetic regulation and post-translational modifications have become emerging directions for neoantigen development[63,65]. Studies show that dysregulation of translational fidelity can generate non-canonical peptides (including antigens from unannotated open reading frames [nuORFs]) via "misreading" events[62]. Notably, while mechanisms of ribosomal RNA methylation (e.g., m4C) in modulating the decoding center are well-characterized in prokaryotes, the association between such modifications and neoantigen diversity in eukaryotic systems, particularly the tumor immune microenvironment, remains unknown[68,69].

Our previous studies revealed that METTL5, an m6A methyltransferase catalyzing adenosine 1832 modification in 18S rRNA, plays a crucial role in tumorigenesis[70]. METTL5 copy number amplification is common across multiple cancers, and METTL5 depletion generates neoantigens through non-canonical frame translation. This unexpected mechanism expands both the diversity and sources of tumor neoantigens, offering a novel pathway to enhance anti-tumor immune responses. Based on these findings, this study integrates multi-omics analysis with functional validation to demonstrate, for the first time, that METTL5-mediated m6A modification in ribosomes restricts neoantigen generation by precisely regulating translational fidelity. Furthermore, we developed a reversible immunotherapeutic strategy targeting this pathway, providing an innovative solution to overcome tumor immune editing.

124 **RESULTS**

125 **METTL5 is identified as a negative regulator of tumor immunogenicity**

126 Based on multi-omics data analysis from the ROCPOT immunogenomics platform, we
127 systematically compared the differential expression profiles of 11 key translation
128 regulatory factors between immune checkpoint blockade (ICB) therapy responders
129 (n=82) and non-responders (n=72). Screening results revealed that multiple translation
130 regulatory factors participate in tumor immune regulation (Fig. 1A). Notably,
131 Fibrillarin (FBL) plays a significant role in tumorigenesis, progression, drug resistance,
132 and immune evasion, with its overexpression typically associated with aggressive
133 tumor phenotypes and poor prognosis[71,72]. Additionally, the expression levels of
134 METTL5 and TRMT112 showed significant negative correlation with ICB treatment
135 response. Our previous research demonstrated that METTL5 must form a functional
136 heterodimeric complex with TRMT112 to catalyze m^6A methylation of adenosine at
137 position 1832 in 18S rRNA[73]. This suggests that m^6A1832 modification in 18S rRNA
138 may serve as the key molecular mechanism by which the METTL5-TRMT112 complex
139 regulates tumor immunity. These findings indicate that targeting translation regulatory
140 mechanisms may represent a novel strategy for optimizing immunotherapy, offering
141 potential therapeutic avenues to overcome ICB resistance.

142

143 **METTL5 loss alters tumor growth in syngeneic models**

144 To evaluate the functional role of METTL5 in tumor immunogenicity, we generated
145 *Mettl5*-knockout B16-F10 melanoma and 4T1 breast cancer cell lines using
146 CRISPR/Cas9-mediated gene editing (Fig. S1A). Sanger sequencing confirmed
147 biallelic frameshift mutations at the *Mettl5* locus, with indel events clustered around
148 the gRNA target site (Fig. S1A). Quantitative Reverse Transcription PCR (RT-qPCR)
149 demonstrated significant transcript depletion (>70%) in both Mettl5-KO cell lines (Fig.
150 S1B). Furthermore, high-performance liquid chromatography-mass spectrometry
151 (HPLC-MS) quantification revealed complete abrogation of m^6A modification activity
152 in Mettl5-KO cells (Fig. S1C). We first performed in vitro characterization of Mettl5-

153 KO tumor cells. Proliferation kinetics assessed by real-time cell analysis showed no
154 significant differences between Mettl5-KO and scrambled control (SCR) in either cell
155 line (Fig. 1C). Similarly, clonogenic survival assays similarly demonstrated
156 comparable colony-forming abilities (Fig. S1D, S1E). These findings suggest that the
157 loss of METTL5 does not impair the proliferative capacity of tumor cells *in vitro*.
158 To determine the immunological consequences of METTL5 depletion, we established
159 syngeneic tumor models in immunocompromised (nude) and immunocompetent
160 (C57BL/6N and Balb/c) mice. METTL5 deficiency did not influence the ability of B16-
161 F10 cells to form tumors in nude mice, which do not have mature T cells (Fig. 1B).
162 However, when METTL5 deficient cells were inoculated into syngeneic mouse hosts,
163 their abilities to form tumors were significantly attenuated by comparison with SCR
164 cells (Fig. 1D, E). Subsequently, we employed flow cytometry to compare the
165 proliferation of GFP-labeled Mettl5-KO and mCherry-labeled SCR B16-F10 cells
166 under both *in vitro* and *in vivo* conditions. The results demonstrated that METTL5
167 deficient cells exhibited preferential growth suppression compared to control cells (Fig.
168 1F-H), which is consistent with the aforementioned findings. Collectively, METTL5
169 loss attenuates tumor growth in immunocompetent mice, indicating an immune-
170 dependent mechanism for its anti-tumor function.
171
172 **METTL5 knockout enhances tumor immune cell infiltration**
173 To elucidate the mechanism underlying METTL5 deficiency suppresses tumor growth
174 specifically in immunocompetent hosts, we systematically characterized immune cell
175 dynamics within the tumor microenvironment (TME). Immunohistochemical (IHC)
176 analysis of B16-F10 and 4T1 tumors revealed significantly enhanced $CD8\alpha^+$ T cell
177 infiltration in Mettl5-KO lesions compared to SCR controls (Fig. 2A, B). To
178 quantitatively profile immune populations, we isolated leukocytes from B16-F10
179 tumors using Percoll gradient centrifugation followed by multicolor flow cytometry.
180 Mettl5-KO tumors exhibited marked increases in $CD8\alpha^+$ T cells (Fig. 2C, D),

181 accompanied by elevated proportions of NK cells and TH cells (Fig. 2C, D). These
182 findings were corroborated by spleen immunophenotyping, which demonstrated
183 expanded CTL populations in Mettl5-KO tumor-bearing mice (Fig. 2E, F). To
184 investigate transcriptional alterations in Mettl5-KO tumors, we performed single-cell
185 RNA sequencing (scRNA-seq) on freshly isolated tumor tissues (Fig. 2G).
186 Unsupervised clustering identified major immune subsets including $CD8\alpha^+$ T cells, B
187 cells, macrophages, and dendritic cells (Fig. 2H). Notably, the TMEs of Mettl5-KO
188 tumor contained higher proportions of $CD8\alpha^+$ T cells and B cells compared to controls
189 (Fig. 2H-J). However, technical limitations during sample transportation restricted
190 dataset depth, preventing comprehensive subset analysis. Nevertheless, scRNA-seq
191 data consistently validated the immunostimulatory phenotype observed through IHC
192 and flow cytometry, reinforcing METTL5's regulatory role in tumor-immune
193 interactions.
194
195 **Inhibition of METTL5 improves immunotherapy**
196 Given that METTL5 inhibition has been shown to enhance tumor-infiltrating capacity
197 of $CD8\alpha^+$ T cells, which play a critical role in antitumor immunity[74], we further asked
198 whether METTL5 targeting could potentiate immunotherapy. To determine whether
199 METTL5 depletion synergizes with immune checkpoint blockade, we evaluated the
200 combinatorial efficacy of Mettl5-KO and anti-PD-1 therapy in syngeneic tumor models.
201 In C57BL/6N mice bearing B16-F10 melanomas, Mettl5-KO tumors exhibited
202 significantly reduced growth compared to SCR controls following anti-PD-1 treatment
203 (Fig. 3A). The combination of METTL5 inhibition and anti-PD-1 therapy demonstrated
204 the most robust antitumor effect, with median survival prolonged by 3 days relative to
205 single-agent groups (Fig. 3A). These findings were recapitulated in the PD-1-resistant
206 4T1 breast cancer model. Mettl5-KO 4T1 tumors treated with anti-PD-1 showed
207 enhanced therapeutic responses, including reduced tumor volumes, and extended
208 survival compared to other treatment arms (Fig. 3B).

209 To further evaluate the therapeutic efficacy of combinatorial METTL5 inhibition and
210 anti-PD-1 blockade, we analyzed tumor-infiltrating immune cells in B16-F10
211 melanoma tissues using flow cytometry (Fig. 3C, Fig. S3A). The results showed that
212 METTL5 depletion synergizes with anti-PD-1 treatment to enhance CD8α$^+$ T and NK
213 cell mediated antitumor immunity. Compared to SCR tumors, Mettl5-KO tumors
214 exhibited higher proportions of CD8α$^+$ T, CD4$^+$ T cells, and NK cells in both
215 normalization methods (Fig. 3D, Fig. S3B). Consistent with previous findings[75], anti-
216 PD-1 therapy expanded tumor-infiltrating cytotoxic immune cell populations, including
217 CD8α$^+$ T cells, and augmented their functional activity (as measured by elevated
218 CD107a expression). Furthermore, Mettl5-KO synergized with anti-PD-1 treatment to
219 further enhance these effects (Fig. 3D, S3B). Together, our results reveal that METTL5
220 knockout potently augments the anti-tumor efficacy of anti-PD-1 treatment, suggesting
221 that METTL5 inhibition could overcome immune checkpoint inhibitor resistance and
222 improve therapeutic outcomes in cancer immunotherapy.
223

224 **METTL5 knockout specifically enhances aberrant protein expression by**
225 **decreasing ribosomal translation fidelity**

226 METTL5 has been identified as the primary methyltransferase responsible for
227 catalyzing m^{6}A1832 modification on 18S rRNA[70,76,77], its precise molecular
228 mechanisms and functional implications under physiological and pathological
229 conditions remain poorly understood, particularly regarding its role in translational
230 regulation. The A1832 site, catalyzed by METTL5, resides in the ribosomal decoding
231 center and exhibits remarkable evolutionary conservation. In E. coli, while A1832
232 remains unmodified, its paired C1402 carries an m^{4}Cm modification that is essential
233 for stabilizing the small ribosomal subunit rRNA structure, facilitating ribosome
234 assembly, and enhancing translation efficiency and fidelity[68,69]. Higher eukaryotes lack
235 m^{4}Cm1402, suggesting functional compensation by the m^{6}A1832 modification at the
236 corresponding position. Thus, we speculate that METTL5 likely regulates translation

237 fidelity. To test this hypothesis, we employed a dual-luciferase reporter system. This
238 system employed mutant plasmids containing either UGA stop codons or ±1 frameshift
239 mutations downstream of the firefly luciferase start codon, to assess firefly luciferase
240 mRNA translation efficiency in SCR and Mettl5-KO cells. In the control group (no
241 mutations), no significant difference was observed in the Firefly/Renilla ratio between
242 SCR and KO cells, indicating that METTL5 knockout does not inherently disrupt basal
243 translation efficiency. However, the expression of firefly luciferase in Mettl5-KO cells
244 was significantly higher than that in SCR cells under mutant conditions (Fig. 4A, B).
245 Specifically, the UGA stop codon group demonstrated increased ribosomal readthrough
246 of termination signals, while the -1/+1 frameshift mutation groups revealed a reduced
247 ability of ribosomes to correct frameshift errors. These results directly support the
248 notion that METTL5 knockout decreases ribosomal translation fidelity, manifesting as
249 enhanced tolerance to termination signal readthrough and frameshift errors, thereby
250 promoting the expression of aberrant proteins encoded by mutant plasmids.
251

252 **Loss of METTL5 enhances immunogenic neoantigen production via non-**
253 **canonical ORF translation**

254 Given the observed translational perturbations in Mettl5-KO cells, we hypothesized
255 that METTL5 deficiency might impair translational fidelity, potentially leading to
256 increased translation of non-canonical open reading frames (nuORFs). This could
257 promote tumor neoantigen generation and consequently enhance tumor
258 immunogenicity. Unlike conventional gene mutations (which are restricted by central
259 tolerance mechanisms and thus fail to elicit strong immune responses), nuORFs may
260 represent more promising novel antigen targets[63,65]. To test this hypothesis, we first
261 performed hierarchical prediction of translated nuORFs in Mettl5-KO versus SCR
262 tumor cells using ribosome profiling (Ribo-seq) (Fig. S3A, S4B). The prediction
263 strategy was as follows (Fig. 4C): The actively translated ORFs were categorized into
264 annotated ORFs and nuORFs, and nuORFs were further classified into shared nuORFs

265 (expressed in both groups with a TPM difference of less than 1.5-fold between the two
266 groups), KO-specific nuORFs (present only in the KO group or with a TPM exceeding
267 that in the SCR group by 1.5-fold), and SCR-specific nuORFs (present only in the SCR
268 group or with a TPM exceeding that in the KO group by 1.5-fold). Subsequently, all
269 nuORFs were categorized into five subtypes[65]: novel ORFs, uORFs (upstream ORFs),
270 dORFs (downstream ORFs), overlap_uORFs (overlapping upstream ORFs), and
271 overlap_dORFs (overlapping downstream ORFs) (Fig. 4D). Further analysis revealed
272 that nuORFs primarily originate from protein-coding genes, pseudogenes, and long
273 non-coding RNAs (lncRNAs) (Fig. S4C). In contrast to annotated ORFs, nuORF
274 translation initiation is heavily dependent on non-canonical start codons-particularly
275 CUG (Fig. S4D)-implying active translation in non-coding genomic regions.
276 Furthermore, the polypeptides translated from nuORFs are significantly shorter than
277 those produced by annotated ORFs (Fig. S4E). Analysis revealed that while METTL5
278 knockout had minimal impact on global translation (Fig. S4F), it significantly enhanced
279 the production of KO-specific novel ORFs (Fig. 4E, Fig. S4G). Besides, the translation
280 efficiency of novel nuORFs in the KO group was higher than that in the SCR group
281 (Fig. S4H), indicating that the extent of translation activation in non-coding regions
282 was much higher in the KO group than in the SCR group. In Ribo-seq data analysis, if
283 the 5' end position of ribosome profiling fragment (RPF) reads meets the condition of
284 being a certain number of base pairs away from the ORF start site such that the base
285 count modulo 3 equals 1, it indicates that the reading frame is correct (frame 0),
286 meaning that the ribosome is translating along the mRNA without a frameshift. Further
287 analysis of reading frame integrity revealed (Fig. 4F) that in the annotated ORF group,
288 the SCR group had a higher in-frame rate than the KO group, suggesting an increased
289 probability of translation frameshifts in the KO group. However, in the nuORF group,
290 the KO group exhibited a significantly higher in-frame rate than the SCR group,
291 indicating that these KO-specific nuORFs were more consistent with the standard

292 triplet codon reading frame, which may imply more efficient translation or more precise
293 start site recognition.
294 To verify whether the high in-frame KO-specific nuORFs are truly translated and
295 whether these nuORFs have the potential to become neoantigens presented by MHC-1,
296 we confirmed the existence of their translation products through MHC-1-IP-MS. Based
297 on the property that neoantigens require a polypeptide length of at least 8 amino acids,
298 we selected nuORFs with amino acid lengths greater than 8 as the reference for the IP-
299 MS database search. Although the number of KO-specific nuORFs was less than that
300 in the SCR group, HPLC-MS search results showed that 165 translation products of
301 KO-specific nuORFs were detected, significantly higher than the 68 detected in the
302 SCR group (Fig. 4G). For example, the peptide sequence NH_2-R-G-P-F-A-D-E-N-F-
303 COOH identified in Mettl5-KO cells, displayed the hallmark 3-nucleotide periodicity
304 of ribosomal translation. Subsequent HPLC-MS analysis confirmed the presence of its
305 amino acid hydrolysis products (Fig. 4H). Together, these findings indicate that
306 METTL5 loss enhances translation of nuORFs.
307
308 **METTL5 deficiency enhances TCR clonal diversity in tumors**
309 Based on our previous findings that METTL5-deficient tumors generate increased
310 neoantigen loads, we hypothesized that METTL5 knockout would drive enhanced T-
311 cell receptor (TCR) repertoire diversity in tumor-bearing hosts. To test this, we
312 performed TCR sequencing on peripheral blood samples from B16-F10 melanoma
313 mouse models at experimental endpoints and conducted comparative TCR repertoire
314 analysis between Mettl5-KO and SCR groups. CDR3 length distribution histograms
315 revealed conserved overall patterns between groups, with dominant peaks observed at
316 10–15 amino acid (aa) lengths (Fig. S4I). Quantitative analysis showed significant
317 differences in TCR repertoire diversity between Mettl5-KO and SCR tumor-bearing
318 mice. The Shannon entropy of the KO group (mean = 11.5) was significantly higher
319 than that of the SCR group (mean = 10.5, $p < 0.05$), indicating greater TCR repertoire

320 diversity in tumor-bearing hosts with METTL5-deficient tumors (Fig. 4I). Furthermore,
321 the clonality index was significantly lower in the KO group compared to the SCR group,
322 suggesting reduced dominance of private clones and a more evenly distributed clonal
323 landscape in METTL5-deficient tumor-bearing mice (Fig. 4J). Diversity estimations
324 across Hill diversity profiles (Q values 0–6) consistently demonstrated higher diversity
325 indices in the KO group (Fig. 4K). Collectively, the above results provide evidences
326 that METTL5-deficient tumors enhance neoantigen-driven T-cell activation. This
327 expanded TCR landscape may improve recognition capacity for heterogeneous
328 neoantigens generated by aberrant translation, potentially strengthening anti-tumor
329 immunity. Together with our prior demonstration of METTL5-dependent translational
330 fidelity regulation, these data establish a mechanistic link between ribosomal RNA
331 modification defects and tumor immunogenicity.
332
333 **METTL5 depletion unveils targetable neoantigens for vaccine-based tumor**
334 **immunotherapy**
335 Building on our prior evidence that METTL5 deficiency enhances MHC-I-restricted
336 neoantigen presentation, we hypothesized that genetic ablation of β2-microglobulin
337 (B2M), a critical component of the MHC class I heterodimer, would abolish the
338 antitumor effects observed in METTL5 deficiency tumors. In order to test this
339 hypothesis, *B2m* was disrupted using the same CRISPR-Cas9 system as for *Mettl5*
340 knockout, and the knockout efficiency was validated by Western blotting (Fig. S5A,
341 S5B). In syngeneic tumor models, we compared the growth kinetics of tumors derived
342 from *METTL5-B2M* double-knockout cells and *B2M*-knockout scramble control cells
343 (Fig. 5A). Both groups exhibited comparable tumor growth rates throughout the
344 experimental period, with no statistically significant differences in tumor volume. In
345 contrast, the Mettl5-KO single-target group recapitulated the tumor growth suppression
346 previously observed, confirming the specificity of the antitumor phenotype. Survival
347 analysis further corroborated these findings. These data definitively establish that

348 MHC-I-dependent antigen presentation is indispensable for the antitumor immunity
349 elicited by METTL5 depletion.
350 Based on neoantigen sequences identified through Ribo-seq and MHC-I-IP-MS
351 analyses of Mettl5-KO tumors, we developed peptide-based and mRNA-based
352 vaccines targeting these epitopes. Their therapeutic potential was evaluated in
353 syngeneic B16-F10 tumor models. Longitudinal tumor monitoring revealed that the
354 SCR+Poly(I:C)+peptide group exhibited significantly suppressed tumor growth
355 compared to the SCR+Poly(I:C) control group (Fig. 5B). Survival analysis further
356 demonstrated that median survival extended from 28 days (SCR+Poly(I:C)) to 35 days
357 in vaccinated mice (SCR+Poly(I:C) + peptide), confirming the protective immunity
358 elicited by METTL5-related neoantigens. Similarly, mRNA vaccines encoding these
359 neoantigen sequences showed robust antitumor effects, with the
360 SCR+liposome+mRNA group displaying significantly reduced tumor volumes
361 compared to the liposome-only control (SCR+liposome) (Fig. 5C). However, these
362 therapeutic benefits were not observed in Mettl5-KO tumors, where neither peptide nor
363 mRNA vaccines further improved survival or tumor suppression.Flow cytometry
364 analysis revealed differences in immune cell infiltration(Fig. S5C). Vaccination
365 significantly increased intratumoral $CD8^+$ T cell proportions in control tumors
366 (SCR+liposome+mRNA vs. SCR+liposome), whereas Mettl5-KO tumors showed no
367 $CD8^+$ T cell enrichment regardless of vaccination status (KO+liposome+mRNA vs.
368 KO+liposome). NK cell dynamics followed a similar trend, with vaccinated control
369 tumors exhibiting approximately a two-fold increase in NK cell infiltration compared
370 to controls. In contrast, Mettl5-KO tumors-maintained baseline NK cell levels
371 irrespective of treatment. These observations are consistent with an association between
372 METTL5 deficiency and altered immune cell infiltratin dynamics, though causality
373 remains undetermined.
374
375

376 **MATERIALS AND METHODS**

377 **Cell culture**

378 The B16-F10 melanoma cells and 4T1 breast cancer cells were purchased from Wuhan
379 Pricella Biotechnology. All cells were authenticated by STR profiling and testing for
380 mycoplasma contamination was performed with a MycAway one-step mycoplasma
381 detection kit (Yeasen, 40612ES25). All cells were cultured in Dulbecco's Modified
382 Eagle Medium (DMEM, Gibco) supplemented with 10% fetal bovine serum (FBS,
383 Biological Industries), 1% penicillin-streptomycin (Thermo Fisher Scientific), and 1%
384 SaveIt mycoplasma inhibitor (Hanbio Biotechnology). Cells were maintained in a
385 humidified incubator at 37°C with 5% CO_2 and routinely tested for bacterial and
386 mycoplasma contamination.

387

388 **Plasmid construction and Generation of knockout cell**

389 Knockout cells were generated using CRISPR/Cas9 technology. Two independent
390 sgRNAs (targeting *Mettl5* or *B2m* exon 2) were cloned into pL-CRISPR.EFS.GFP
391 plasmid separately. To generate *Mettl5* knockout cells, 2 μg of sgRNA vector that
392 targeting mouse *Mettl5* was transfected to the corresponding cells using Lipofectamine
393 3000 (Invitrogen). After 2 days' culture in DMEM medium, cells were screened
394 according to fluorescence and isolated into monoclons by flow cytometry. After 3
395 weeks' culture, colonies were screened out and confirmed by sequencing and RT-qPCR.
396 LCMS/MS was also used to further detected the changes of m^6A modification in SCR
397 and *Mettl5-KO* cells. To generate *Mettl5*-knockout plus *B2m* knockout B16F10 cells, 2
398 μg of sgRNA vector that targeting mouse *B2m* was transfected to B16 SCR or *Mettl5-*
399 *KO* cells using Lipofectamine 3000 (Invitrogen). After 2 days' culture in DMEM
400 medium, cells were screened according to fluorescence and isolated into monoclons by
401 flow cytometry. After 3 weeks' culture, colonies were screened out and confirmed by
402 western blot.

403 sgRNA sequences targeting mouse *Mettl5* locus:

404 AGCATCGGAGCGGCAATGCT

405 sgRNA sequences targeting mouse *B2m* locus:

406 AGTATACTCACGCCACCCACCGG

407

408 **Cell proliferation and colony formation**

409 For cell proliferation, 1.5 × 10^5 cells were seeded in a 24-well plate on day 0 and
410 counted on day one until day 3 with a cell counter (Thermo Fisher Scientific) to measure
411 cell proliferation. For colony formation, 500 cells were seeded in a 6-well plate and
412 cultured for six days. Cells were then fixed with 4% formaldehyde (Beyotime) and
413 stained with 0.1% crystal violet solution (Solarbio). Next, the number and size of Cell
414 colonies were measured.

415

416 **Western blot**

417 For western blotting, a six-well plate of cells at approximately 80-90% confluency was
418 lysed with 100 μl RIPA buffer on ice. Cell lysates were separated by 4-20% SDS-PAGE,
419 and the protein was then transferred to 0.4 μm polyvinylidene fluoride (PVDF, Merck
420 Millipore) membrane. After blocking with 5% milk in TBST, the membranes were then
421 incubated with the corresponding antibodies overnight at 4°C. Membranes were
422 incubated with secondary HRP-conjugated antibody (Proteintech) at room temperature
423 for 2 hours following three times washes with TBST and were washed three times again
424 before detected by the phosphoimager. The corresponding antibodies included
425 Monoclonal rabbit anti-B2m antibody with 1:5000 dilution (Abcam, ab75853) and
426 anti-GAPDH antibody with 1:5000 dilution (Proteintech, 10494-1-AP).

427

428 **Quantitative Reverse Transcription PCR (RT-qPCR)**

429 Total RNA was isolated from B16F10 and 4T1 cells using Total RNA Isolation Kit
430 (Vazyme) and reverse-transcribed to cDNA by the use of RT reagent Kit (TaKaRa).
431 Reactions were run on the real-time PCR machine (QuantStudio 7 Flex) using TB

432 Green PCR master- mix (TaKaRa). The relative gene expression level was calculated
433 with the comparative cycle threshold (CT) method, and the relative number of target
434 transcripts was normalized according to mouse GAPDH gene. Each experiment was
435 performed in triplicate.
436 METTL5:
437 Forward primer: 5'- CTGAAGACTGCTTTGGGAATGGC-3';
438 Reserve primer: 5'- AATGCTGGTAGATCATATCGAAGC-3'.
439 GAPDH:
440 Forward primer: 5'-CATCACTGCCACCCAGAAGACTG-3';
441 Reserve primer: 5'- ATGCCAGTGAGCTTCCCGTTCAG-3'.
442
443 **Animal Sources**
444 Six- to 8-week-old female C57BL/6N mice were purchased from Beijing Vital River
445 Laboratory Animal Technology Co., Ltd. Six- to 8-week-old female Balb/c mice and
446 3- to 4-week-old female nude mice were obtained from GemPharmatech. All mice were
447 bred in a specific-pathogen-free (SPF) animal facility with a 12-h light/12-h dark cycle,
448 at 22.5 ± 1°C and 50 ± 5% relative humidity. All animal experiments were approved
449 by the Institutional Animal Care and Use Committee (IACUC) of Southern University
450 of Science and Technology.
451
452 **In vivo competition assay**
453 For generation of mCherry-labeled SCR and GFP-labeled Mettl5 knockout KO cells,
454 lentiviral particles were produced by co-transfecting 293T cells with either the GFP or
455 mCherry plasmid along with the packaging plasmids pMD2.G and PsPAX2. SCR B16
456 cells were transduced with the GFP-expressing lentivirus, while Mettl5-KO cells were
457 infected with the mCherry-expressing lentivirus. Following three days of culture, cells
458 were fluorescence-sorted by flow cytometry to isolate stable populations expressing the
459 respective markers. A 1:1 mixture of mCherry-labeled SCR cells and GFP-labeled KO

460 cells was prepared. This mixture was either subcutaneously injected into C57BL/6N
461 mice or co-cultured in vitro. Tumors were harvested 12 days post-injection, and the
462 relative proportions of GFP^+ (Mettl5-KO) and $mCherry^+$ (SCR) cells in both tumors
463 and in vitro cultures were quantified by BD Canto II flow cytometer (Flow Cytometry
464 Shared Facility, SUSTech University).
465
466 **Tumour growth in mice**
467 Syngeneic and xenogeneic subcutaneous tumor transplantation assays to evaluate
468 tumorigenicity of mettl5-deficient tumor cells. For syngeneic models, tumor cells were
469 resuspended in PBS (Gibco) and injected subcutaneously into the right dorsal flank of
470 C57BL/6N or Balb/c mice. For xenogeneic models, tumor cells were mixed with an
471 equal volume of Matrigel (Corning) at a 1:1 ratio before subcutaneous injection into
472 nude mice. Tumor volume was measured every other day starting from day 5 or 7 until
473 tumors reached a maximum size of 2000 mm^3, calculated as length × $width^2$. At the
474 experimental endpoint, tumors were harvested and weighed.
475
476 **Preparation of tumor tissue single-cell suspension**
477 At the endpoint of the mouse tumor model, tumors were bluntly dissected intact using
478 surgical scissors and forceps (RWD). After all tumors were stripped, the mass of each
479 tumor sample was recorded and transferred to a 6-cm dish with appropriate HBSS
480 (Gibco). Using curved scissors (RWD), tumors were uniformly minced until passable
481 through a 1-ml pipette tip. Then, collagenase IV (0.5 mg/ml, Sigma) and DNase I (100
482 U/ml) were added proportionally to the tumor volume. Digestion was performed on a
483 37°C shaker at 80 rpm for 45 min. The tumor suspension was filtered through a 70-μm
484 strainer, and single-cell suspension was obtained by centrifugation at 1500 rpm for 10
485 min at 4°C, followed by three PBS washes. Finally, cells were collected, stained with
486 antibodies, and analyzed by flow cytometry.
487

488 **Analysis of tumour-infiltrating lymphocytes**

489 Single-cell suspensions of tumor tissues were prepared and incubated with 50 μL of a
490 solution containing anti-mouse CD16/32 (BioLegend, catalog #101320, diluted 1:50)
491 and anti-mouse Zombie NIR™ Fixable Viability Kit (APC-750, BioLegend, catalog
492 #423105, diluted 1:200) to block non-specific binding and label dead cells. After
493 incubation at 4°C for 10 minutes, a cocktail of surface antibodies for mouse immune
494 cell subset staining was prepared. Cells were stained with the antibody cocktail in 100
495 μL of tumor staining buffer (BioLegend, #420201) on ice at 4°C for 30 minutes. After
496 incubation, cells were washed twice with staining buffer and resuspended in 900 μL of
497 staining buffer. Counting beads (Invitroge) were added (100 μL per sample) to quantify
498 cell concentrations. Samples were analyzed using a BD Canto II flow cytometer (Flow
499 Cytometry Shared Facility, SUSTech University), with 300,000 $CD45^+$ events recorded
500 per sample. Data were analyzed using FlowJo (version 10).

501 The antibodies used were as follows: anti-mouse CD4 (Pacific Blue, BioLegend,
502 #100531, diluted 1:200); anti-mouse CD45 (Brilliant Violet 510, BioLegend, #103138,
503 diluted 1:100); anti-mouse CD19 (FITC, BioLegend, #115505, diluted 1:200); anti-
504 mouse CD8a (PerCP/Cyanine5.5, BioLegend, #100734, diluted 1:200); anti-mouse
505 NK-1.1 (PE, BioLegend, #108708, diluted 1:200);anti-mouse CD25 (PE/Dazzle 594,
506 BioLegend, #102048, diluted 1:200); anti-mouse TCR β chain (PE/Cyanine7,
507 BioLegend, #109222, diluted 1:200); anti-mouse CD107a (APC，BioLegend, #121615，
508 diluted 1:200); anti-mouse CD11c (APC/Fire™ 750, BioLegend, #117352, diluted
509 1:200).

510

511 **Immunohistochemistry (IHC) detection**

512 IHC was used to evaluate the expression of CD8α in tumor tissues and compare SCR
513 and Mettl5-KO samples. Paraffin-embedded tumor tissues were sectioned into 4-5 μm
514 thick slices and mounted on glass slides. The sections were deparaffinized using xylene
515 and alcohol, followed by antigen retrieval in a citrate buffer. Nonspecific binding was

516 blocked with an appropriate solution, and then a primary antibody specific to the CD8α
517 protein was applied and incubated overnight at 4°C. After washing, a secondary HRP-
518 conjugated antibody was added and incubated for one hour at room temperature. The
519 bound antibodies were visualized using an IHC detection substrate that produced a
520 colorimetric reaction. Counterstaining with hematoxylin was performed to highlight
521 cell nuclei. Images were captured using a microscope, and positive staining cells were
522 quantified within a defined area using image analysis software. Statistical analysis was
523 conducted to assess the differences in the number of stained cells between SCR and KO
524 samples, and the findings were reported with representative images, quantitative data,
525 and a discussion of the results.
526
527 **Luciferase Reporter Assay**
528 we employed a dual luciferase reporter assay using the pmirGLO vector, which
529 contains both firefly (F-Luc) and Renilla (R-Luc) luciferases. The activity of F-Luc,
530 normalized to R-Luc activity, was used to evaluate the reporter translation efficiency.
531 Specifically, mutation plasmids were engineered by introducing a UGA stop codon and
532 frameshift mutations (+1 or -1) into the firefly luciferase gene. In contrast, the wild-
533 type (WT) plasmid did not contain these mutations, thus maintaining the normal firefly
534 luciferase sequence. B16-F10 cells, both WT and METTL5 KO, were transfected with
535 1 μg of either the empty vector or mutation reporter plasmid. After 48 hours post-
536 transfection, luciferase expression was measured using the Dual-Glo Luciferase Assay
537 System (Promega).
538
539 **Ribo-seq**
540 Two 15-cm plates of cells with approximately 80-90% confluency was used per group.
541 Cells were incubated with 100 μg/ml Cycloheximide (MCE) for 8 min at 37°C and
542 were then lysed on ice for 10min in 400uL lysis buffer (20 mM Tris–HCl pH 7.5, 150
543 mM NaCl, 5 mM $MgCl_2$, 1 mM DTT, 100 μg/ml Cycloheximide, 1% Triton X-100).

544 The supernatant was collected via centrifugation at 12 000 g for 10 min at 4 °C, and its'
545 absorbance at 260nm was measured. The ribosomes with equal A260 in each group
546 were reserved for RNA sequencing. Added 15U RNase1 (Thermo Fisher Scientific) for
547 each 1OD of lysate, and incubated the reactions at 22°C for 40 min with gentle mixing.
548 Ribosome-protected fragments (RPFs) were collected by MicroSpin S-400 columns
549 (Cytiva) and purified by Zymo Research RNA Clean & Concentrator-25 kit (Zymo).
550 The RPFs were then separated with 15% polyacrylamide TBE–urea gel, excised the gel
551 slices between 17 and 34 nucleotides and recovered RNA from PAGE gel by ZR small-
552 RNA™ PAGE Recovery Kit (Zymo). Purified RNA was treated with PNK(NEB), and
553 the RNA library was prepared by VAHTSTM Small RNA Library Prep Kit for
554 Illumina®(Vazyme). The library concentration was analyzed using the VAHTSTM
555 Library Quantification Kit for Illumina®, and equimolar pools of libraries were
556 sequenced.
557
558 **MHC peptide enrichment**
559 For MHC peptide isolation, four 15-cm plates of B16 SCR or Mettl5-KO cells were
560 harvested and subsequently lysed on ice in 8 mL of 1× Lysis buffer (comprising 0.5%
561 NP-40, 50 mM Tris pH 8.0, 150 mM NaCl, and protease inhibitor) for 10 minutes.
562 Following lysis, protein extracts were obtained by centrifugation at 12,000 g for 10
563 minutes at 4°C. The supernatants were then incubated overnight with anti-mouse MHC-
564 I antibody conjugated to Pierce Protein A/G magnetic beads (Santa Cruz) to facilitate
565 immunoprecipitation. The bead-protein mixture was first treated with 1 mL of Wash
566 Buffer 1 (0.5% NP-40, 50 mM Tris-HCl pH 8.0, 150 mM NaCl, 5 mM EDTA, 100 μM
567 PMSF, and protease inhibitor) to remove nonspecifically bound proteins while
568 simultaneously inhibiting proteolytic degradation. Subsequent washes included 1 mL
569 of Wash Buffer 2 (50 mM Tris-HCl pH 8.0, 150 mM NaCl) to eliminate residual
570 detergent from the first step. High-affinity contaminants were then dissociated using 1
571 mL of Wash Buffer 3 (50 mM Tris-HCl pH 8.0, 450 mM NaCl), which applied high

572 ionic strength to disrupt non-specific interactions. Finally, a salt-free wash with 1 mL
573 of Wash Buffer 4 (50 mM Tris-HCl pH 8.0) ensured complete removal of residual salts,
574 thereby maintaining compatibility with downstream elution steps. Bound peptides were
575 released by treating the beads with 10% acetic acid (pH ~3.0), which denatures MHC
576 molecules and facilitates peptide dissociation. The eluate was then filtered through a 3
577 kDa molecular weight cut-off filter to remove the MHC-I α-chain, B2m protein, and
578 the corresponding MHC antibody. The eluted proteins were ultimately analyzed by
579 HPLC-MS to identify the MHC peptides. Acid elution was performed on six 15 cm
580 dishes of B16 control cells or B16- Mettl5-KO cells stimulated with 100IU/ml IFN-γ
581 for 24h. Cells were treated on ice with pH3.3 citric acid-phosphate buffer for 5min to
582 dissociate MHC-antigen peptide complexes and release antigenic peptides. After
583 centrifugation at 10000g, the supernatant was collected and filtered through a 3 kDa
584 molecular weight cutoff filter. The eluted proteins were analyzed by HPLC-MS for
585 MHC peptides.
586
587 **TCR library construction and TCRβ sequencing**
588 PBMCs were isolated from whole blood of C57BL/6N mice that had been inoculated
589 with either control B16F10 cells or Mettl5-KO cells 12 days prior. DNA was extracted
590 from PBMC using a QIAamp DNA Blood Mini Kit (Qiagen), and the concentration
591 was tested using NanoDrop 2000 spectrophotometer (Thermo Fisher Scientific). The
592 DNA was used as a template for PCR amplification, which was performed to generate
593 the library of TCR and BCR. The step 1 PCR amplification protocol was as follows:
594 95 °C for 5 min; 95 °C for 30 s, 59 °C for 30 s; 72 °C for 1 min for 30 cycles; and 72 °C
595 for 10 min. The step 2 PCR amplification protocol was as follows: 98 °C for 2 min;
596 98 °C for 30 s, 65 °C for 30 s; 72 °C for 30 s for 10 cycles; and 72 °C for 5 min. The
597 PCR products were purified, and the barcodes were confirmed. The annealed region of
598 these primers was the CDR3 region, as shown by Multiplex PCR Amplifies. The CDR3
599 regions were sequenced on Illumina NextSeq500 (MyGenostics). According to the

600 sequencing depth, the test covered about 90% of the TCR. The CDR3 regions were
601 identified based on the definition established by the International ImMunoGeneTics
602 (IMGT) (http://www.imgt.org/, accessed on 19 March 2021) collaboration, and the V,
603 D, and J segments contributing to each CDR3 region were identified by a standard
604 algorithm. Data were analysed using ImmunoSEQ Analyzer 3.0, an Adaptive
605 Biotechnologies online analysis platform.
606
607 **RNA-seq and ribo-seq analysis**
608 Adapter sequences were removed from both Ribo-seq and RNA-seq reads using
609 TrimGalore (v0.6.7). For Ribo-seq data, reads shorter than 20 nucleotides or longer
610 than 35 nucleotides were discarded to ensure high-quality ribosome-protected fragment
611 selection. The trimmed reads were then aligned to rRNA and tRNA sequences using
612 Bowtie2 (v2.2.5)[78]. Reads that aligned to rRNA or tRNA were excluded, while the
613 remaining unaligned reads were retained for subsequent analysis. Processed reads were
614 aligned to the reference genome (gencode GRCh38) by the STAR (v2.7.10a)[79],
615 allowing for at most two mismatches. For Ribo-seq data, quality control and
616 translational profiles was analyzed by RiboseQC. Transcriptome assembly and
617 quantification were performed using StringTie (v2.1.7)[80]. Both read counts of Ribo-seq
618 and RNA-seq were converted to TPM (transcripts per million). Genes with sufficient
619 expression level (Ribo TPM > 1 and RNA TPM > 5) were subjected to further analysis.
620 Translation efficiency (TE) and the differentially-TE genes (DTEGS) were calculated
621 by RiboDiff (v0.2.2)[81], GO term analysis were performed by Metascape
622 (https://metascape.org/gp/index.html). GraphPad Prismsoftware and R was used for
623 data presentation.
624
625 **Hierarchical prediction of translated ORFs across tissues**
626 In our study, we used the RiboCode[82] algorithm to detect actively translated open
627 reading frames (ORFs) with the parameters set as follows: a minimum fractional

threshold of ribosome profiling reads (-f0_percent 0.5), a primary start codon of ATG (--start_codon ATG), alternative start codons of CTG, GTG, and TTG (--alt_start_codons CTG, GTG, TTG), and a minimum amino acid length of 8 (--min-AA-length 8). The identified ORFs were classified into several categories: "annotated" ORFs, which overlap with annotated coding sequences (CDS) and share the same stop codon; "uORFs", located upstream of the annotated CDS without overlap; "dORFs", situated downstream of the annotated CDS without overlap; "Overlap_uORFs", overlapping with the annotated CDS while being upstream; "Overlap_dORFs", overlapping with the annotated CDS while being downstream; "Internal" ORFs, which are internal to the annotated CDS but in a different reading frame; and "novel" ORFs, originating from non-coding genes or non-coding transcripts of coding genes. Additionally, we generated collapsed BED12 files for annotated ORFs (annotatedORFdb.bed) and non-canonical ORFs (excluding the “annotated” type, nuORFdb.bed), which served as references for subsequent analysis.

Generating nuORFdb v.1.0

To count the number of ribosomal profiling (RPF) reads aligned to ORFs, we first corrected the read positions based on the offset distances between the 5' end of the reads and the ribosomal A-sites. Subsequently, we employed the “rpfTPM” script from a prior study (available at link) to quantify the number of in-frame reads. This script normalizes the in-frame read counts to transcripts per million (TPM) against the nuORFdb.bed file. ORFs with TPM values 1.5-fold higher in the KO samples compared to SCR samples were designated as “KO-larger nuORFs”. Conversely, ORFs with TPM values 1.5-fold higher in SCR samples relative to KO samples were classified as “SCR-larger nuORFs”. Please note that the link to the script could not be parsed due to network issues. If needed, please verify the link's validity and try accessing it again. If you don't require the content from this link, the rest of your request has been addressed as follows.

656

657 **Estimation of absolute translation levels**

658 UniProt (reviewed mouse, release 2025_02) and the translated amino acid sequences
659 of larger nuORFs were used as reference databases for protein and peptide
660 identification. Notably, only those nuORFs longer than 8 aa were defined as potential
661 translated regions. The proteomics search was performed using SearchGUI (v4.2.17)
662 (https://github.com/compomics/searchgui) with MS-GF+ and Tide as search engines.
663 Carboxyamidomethylation of cysteine was set as a fixed modification, while oxidation
664 of methionine and proline were set as variable modifications. The enzyme specificity
665 was set to 'unspecific' and the precursor mass tolerance was set to 20 ppm
666 Hydrophobicity values for total PSM peptides were predicted with R package protViz
667 (v0.7.9) (https://github.com/cpanse/protViz).

668

669 **Statistical analysis**

670 No sample size calculations and blinding were performed. There was no method of
671 randomization. No samples or animals were excluded from analysis. Prism 9 software
672 (GraphPad) was used to analyze data from biological experiments by performing two-
673 tailed unpaired Student's t-tests. One-way analysis of variance (ANOVA) with Tukey's
674 test was used to compare multiple groups and two-way ANOVA was used to compare
675 cell proliferation analysis and tumor growth curves. P values $^{*}P<0.05$, $^{**}P<0.01$,
676 $^{***}P<0.001$, $^{****}P<0.0001$ were considered statistically significant.

677

678

679 **DISCUSSION**

680 This study reveals METTL5 as a central ribosomal translation regulator in tumor
681 immune evasion through integrated multi-omics analysis and functional validation.
682 METTL5 depletion markedly enhances tumor neoantigen burden by activating
683 noncanonical upstream open reading frame (nuORF) translation. This mechanism
684 fundamentally differs from traditional mutation-derived neoantigens, as its origin relies
685 not on genomic mutation accumulation but dynamically expands antigenic diversity
686 through translational fidelity regulation, providing a novel strategy to overcome
687 immunotherapy resistance[63,65,67].

688 At the molecular level, METTL5-mediated m^6A1832 modification resides at the h44-
689 h45 helical junction of 18S rRNA, a critical site within the ribosomal decoding center
690 responsible for maintaining codon-anticodon pairing accuracy[70,73,76]. Although m^4C
691 modifications in prokaryotic decoding centers are well-established regulators of
692 translational fidelity[68,69], this study identifies METTL5-catalyzed m^6A modification at
693 the eukaryotic homologous region as a potential functional analog. Cryo-electron
694 microscopy analysis detected two distinct conformational states in the decoding center
695 of METTL5-deficient 293T cells. However, how these structural alterations
696 quantitatively affect translational fidelity in tumor cells remains unclear. Dual-
697 luciferase reporter assays demonstrated increased read-through rates of UGA stop
698 codons and significant elevation of ±1 frameshifting events in METTL5-knockout
699 tumor cells. Ribosome profiling further confirmed enhanced translation initiation at
700 noncanonical start codons in METTL5-deficient cells, with a notable increase in
701 translated peptide lengths exceeding eight amino acids, thereby generating an expanded
702 neoantigen reservoir for MHC-I presentation.

703 In terms of tumor immune microenvironment, METTL5-depleted tumors exhibited a
704 pronounced "hot phenotype". Flow cytometry and single-cell sequencing revealed
705 increased $CD8\alpha^+$ T cell infiltration density, elevated NK cell proportions, and a T cell
706 receptor (TCR) repertoire with a Shannon diversity index of 11.5 compared to 10.5 in

707 controls. Notably, TCR clones from METTL5-knockout tumors showed CDR3 regions
708 preferentially lengthened to 12-14 amino acids, a range associated with enhanced
709 antigen-binding flexibility[83]. In anti-PD-1 combination therapy models, METTL5
710 knockout combined with PD-1 blockade significantly prolonged the median survival of
711 tumor-bearing mice while increasing the proportion of $CD107a^{+}$ cytotoxic T cells and
712 NK cells within the tumor microenvironment[75], demonstrating that translational
713 reprogramming synergizes with checkpoint inhibition to reverse immune exhaustion.
714 Despite these therapeutic implications, clinical translation of METTL5-targeting
715 strategies faces multiple challenges. First, METTL5 depletion did not affect in vitro
716 proliferation of murine melanoma or breast cancer cells, yet its functional context may
717 exhibit tissue- or species-specificity requiring further investigation. Second, reduced
718 translational fidelity risks aberrant self-antigen release; although METTL5 is
719 overexpressed in tumors, long-term autoimmunity monitoring remains necessary. Third,
720 nuORF-based vaccine efficacy is constrained: in B16-F10 models, MHC-I
721 immunopeptidome analysis using $H2\text{-}K^{b}$ and $H2\text{-}D^{b}$ antibodies only successfully
722 enriched peptides via $H2\text{-}D^{b}$, limiting comprehensive neoantigen identification; acid
723 elution partially compensates but nuORF translation efficiency remains low with
724 unverified immunogenicity. Additionally, the sensitivity threshold of mass
725 spectrometry techniques and database dependency may lead to missed detection of
726 noncanonical peptides[37].
727 Future studies should focus on resolving dynamic conformational changes in the
728 ribosomal decoding center following METTL5 deletion through cryo-electron
729 microscopy to elucidate atomic-level regulatory mechanisms. Development of specific
730 METTL5 inhibitors is required to balance translational stress thresholds against
731 proteostasis disruption. Machine learning platforms should be constructed to prioritize
732 highly immunogenic nuORF-derived neoantigens. This work not only establishes
733 ribosomal chemical modifications as critical mediators of tumor immune surveillance

but also provides experimental evidence for "translational reprogramming" as a novel strategy to overcome current limitations in cancer immunotherapy.

ACKNOWLEDGEMENTS

We would like to thank all members in Hao Chen's Lab for their help and advice in experimental design. The authors would also like to acknowledge the technical support from Hua Li and Lin Lin at SUSTech CRF. This work was supported by Center for Computational Science and Engineering at Southern University of Science and Technology.

FUNDING

This work was supported by National Key Research and Development Program of China (2022YFC2702705), National Natural Science Foundation of China (32170604) and Pearl River Recruitment Program of Talents (2021QN02Y122) to H.C. This work was also supported by Shenzhen Key Laboratory of Gene Regulation and Systems Biology (Grant No. ZDSYS20200811144002008) from Shenzhen Innovation Committee of Science and Technology and Funding for Scientific Research and Innovation Team of The First Affiliated Hospital of Zhengzhou University (ZYCXTD2023004).

CONFLICT OF INTEREST

The authors declare no conflicts of interest.

AUTHOR CONTRIBUTIONS

H.C. designed and conceived the experiments. Y.Y.Z., X.Y.S., R.Q.W. and Y.L.C. performed experiments. Y.C.W. and X.Y.S. analyzed the data. Y.Y.Z., X.Y.S. and H.C. wrote the manuscript. All authors have read and approved the final manuscript.

764 **REFERENCES**

765 1 Gajewski, T. F. *et al.* Immune resistance orchestrated by the tumor
766 microenvironment. *Immunol Rev* **213**, 131-145 (2006).
767 https://doi.org/10.1111/j.1600-065X.2006.00442.x
768 2 Joyce, J. A. & Fearon, D. T. T cell exclusion, immune privilege, and the tumor
769 microenvironment. *Science* **348**, 74-80 (2015).
770 https://doi.org/10.1126/science.aaa6204
771 3 Hegde, P. S. & Chen, D. S. Top 10 Challenges in Cancer Immunotherapy.
772 *Immunity* **52**, 17-35 (2020). https://doi.org/10.1016/j.immuni.2019.12.011
773 4 Sharma, P., Hu-Lieskovan, S., Wargo, J. A. & Ribas, A. Primary, Adaptive, and
774 Acquired Resistance to Cancer Immunotherapy. *Cell* **168**, 707-723 (2017).
775 https://doi.org/10.1016/j.cell.2017.01.017
776 5 Zaretsky, J. M. *et al.* Mutations Associated with Acquired Resistance to PD-1
777 Blockade in Melanoma. *N Engl J Med* **375**, 819-829 (2016).
778 https://doi.org/10.1056/NEJMoa1604958
779 6 McDonald, K. A. *et al.* Tumor Heterogeneity Correlates with Less Immune
780 Response and Worse Survival in Breast Cancer Patients. *Ann Surg Oncol* **26**,
781 2191-2199 (2019). https://doi.org/10.1245/s10434-019-07338-3
782 7 El-Sayes, N., Vito, A. & Mossman, K. Tumor Heterogeneity: A Great Barrier in
783 the Age of Cancer Immunotherapy. *Cancers (Basel)* **13** (2021).
784 https://doi.org/10.3390/cancers13040806
785 8 Weiskopf, K. *et al.* Engineered SIRPalpha variants as immunotherapeutic
786 adjuvants to anticancer antibodies. *Science* **341**, 88-91 (2013).
787 https://doi.org/10.1126/science.1238856
788 9 Chabner, B. A. & Roberts, T. G., Jr. Timeline: Chemotherapy and the war on
789 cancer. *Nat Rev Cancer* **5**, 65-72 (2005). https://doi.org/10.1038/nrc1529
790 10 Ahmed, M. M. *et al.* Harnessing the potential of radiation-induced immune
791 modulation for cancer therapy. *Cancer Immunol Res* **1**, 280-284 (2013).
792 https://doi.org/10.1158/2326-6066.CIR-13-0141
793 11 Pao, W. *et al.* Acquired resistance of lung adenocarcinomas to gefitinib or
794 erlotinib is associated with a second mutation in the EGFR kinase domain. *PLoS*
795 *Med* **2**, e73 (2005). https://doi.org/10.1371/journal.pmed.0020073
796 12 Oh, T. K. *et al.* Long-Term Oncologic Outcomes, Opioid Use, and
797 Complications after Esophageal Cancer Surgery. *J Clin Med* **7** (2018).
798 https://doi.org/10.3390/jcm7020033
799 13 Nelson, D. B. *et al.* Surgical margins and risk of local recurrence after wedge
800 resection of colorectal pulmonary metastases. *J Thorac Cardiovasc Surg* **157**,
801 1648-1655 (2019). https://doi.org/10.1016/j.jtcvs.2018.10.156
802 14 Sakuishi, K. *et al.* Targeting Tim-3 and PD-1 pathways to reverse T cell
803 exhaustion and restore anti-tumor immunity. *J Exp Med* **207**, 2187-2194 (2010).
804 https://doi.org/10.1084/jem.20100643
805 15 Sharma, P. & Allison, J. P. The future of immune checkpoint therapy. *Science*

806 **348**, 56-61 (2015). https://doi.org/10.1126/science.aaa8172
807 16 Topalian, S. L., Taube, J. M., Anders, R. A. & Pardoll, D. M. Mechanism-driven
808 biomarkers to guide immune checkpoint blockade in cancer therapy. *Nat Rev*
809 *Cancer* **16**, 275-287 (2016). https://doi.org/10.1038/nrc.2016.36
810 17 Johnson, D. B., Peng, C. & Sosman, J. A. Nivolumab in melanoma: latest
811 evidence and clinical potential. *Ther Adv Med Oncol* **7**, 97-106 (2015).
812 https://doi.org/10.1177/1758834014567469
813 18 Le, R. Q. *et al.* FDA Approval Summary: Tocilizumab for Treatment of
814 Chimeric Antigen Receptor T Cell-Induced Severe or Life-Threatening
815 Cytokine Release Syndrome. *Oncologist* **23**, 943-947 (2018).
816 https://doi.org/10.1634/theoncologist.2018-0028
817 19 Turtle, C. J. *et al.* CD19 CAR-T cells of defined CD4+:CD8+ composition in
818 adult B cell ALL patients. *J Clin Invest* **126**, 2123-2138 (2016).
819 https://doi.org/10.1172/JCI85309
820 20 Zhu, L. *et al.* Dapl1 controls NFATc2 activation to regulate CD8(+) T cell
821 exhaustion and responses in chronic infection and cancer. *Nat Cell Biol* **24**,
822 1165-1176 (2022). https://doi.org/10.1038/s41556-022-00942-8
823 21 Puig-Saus, C. *et al.* Neoantigen-targeted CD8(+) T cell responses with PD-1
824 blockade therapy. *Nature* **615**, 697-704 (2023). https://doi.org/10.1038/s41586-
825 023-05787-1
826 22 Carreno, B. M. *et al.* Cancer immunotherapy. A dendritic cell vaccine increases
827 the breadth and diversity of melanoma neoantigen-specific T cells. *Science* **348**,
828 803-808 (2015). https://doi.org/10.1126/science.aaa3828
829 23 Borgers, J. S. W. *et al.* Personalized, autologous neoantigen-specific T cell
830 therapy in metastatic melanoma: a phase 1 trial. *Nat Med* **31**, 881-893 (2025).
831 https://doi.org/10.1038/s41591-024-03418-4
832 24 Braun, D. A. *et al.* A neoantigen vaccine generates antitumour immunity in renal
833 cell carcinoma. *Nature* **639**, 474-482 (2025). https://doi.org/10.1038/s41586-
834 024-08507-5
835 25 Danelli, L. Personalized neoantigen therapy for melanoma immunotherapy. *Nat*
836 *Cancer* **5**, 1783 (2024). https://doi.org/10.1038/s43018-024-00850-w
837 26 Ott, P. A. *et al.* An immunogenic personal neoantigen vaccine for patients with
838 melanoma. *Nature* **547**, 217-221 (2017). https://doi.org/10.1038/nature22991
839 27 Ott, P. A. *et al.* A Phase Ib Trial of Personalized Neoantigen Therapy Plus Anti-
840 PD-1 in Patients with Advanced Melanoma, Non-small Cell Lung Cancer, or
841 Bladder Cancer. *Cell* **183**, 347-362 e324 (2020).
842 https://doi.org/10.1016/j.cell.2020.08.053
843 28 Parkhurst, M. *et al.* Adoptive transfer of personalized neoantigen-reactive TCR-
844 transduced T cells in metastatic colorectal cancer: phase 2 trial interim results.
845 *Nat Med* **30**, 2586-2595 (2024). https://doi.org/10.1038/s41591-024-03109-0
846 29 Wang, M. *et al.* Humanized dual-targeting antibody-drug conjugates specific to
847 MET and RON receptors as a pharmaceutical strategy for the treatment of

848 cancers exhibiting phenotypic heterogeneity. *Acta Pharmacol Sin* (2025).
849 https://doi.org/10.1038/s41401-024-01458-7
850 30 Lim, Z. F. & Ma, P. C. Emerging insights of tumor heterogeneity and drug
851 resistance mechanisms in lung cancer targeted therapy. *J Hematol Oncol* **12**,
852 134 (2019). https://doi.org/10.1186/s13045-019-0818-2
853 31 Dash, P. *et al.* Quantifiable predictive features define epitope-specific T cell
854 receptor repertoires. *Nature* **547**, 89-93 (2017).
855 https://doi.org/10.1038/nature22383
856 32 Tran, E. *et al.* Immunogenicity of somatic mutations in human gastrointestinal
857 cancers. *Science* **350**, 1387-1390 (2015).
858 https://doi.org/10.1126/science.aad1253
859 33 Tran, E. *et al.* Cancer immunotherapy based on mutation-specific CD4+ T cells
860 in a patient with epithelial cancer. *Science* **344**, 641-645 (2014).
861 https://doi.org/10.1126/science.1251102
862 34 Lu, Y. C. *et al.* Mutated PPP1R3B is recognized by T cells used to treat a
863 melanoma patient who experienced a durable complete tumor regression. *J*
864 *Immunol* **190**, 6034-6042 (2013). https://doi.org/10.4049/jimmunol.1202830
865 35 Alban, T. J. *et al.* Neoantigen immunogenicity landscapes and evolution of
866 tumor ecosystems during immunotherapy with nivolumab. *Nat Med* **30**, 3209-
867 3222 (2024). https://doi.org/10.1038/s41591-024-03240-y
868 36 Lopez, J. *et al.* Autogene cevumeran with or without atezolizumab in advanced
869 solid tumors: a phase 1 trial. *Nat Med* **31**, 152-164 (2025).
870 https://doi.org/10.1038/s41591-024-03334-7
871 37 Huber, F. *et al.* A comprehensive proteogenomic pipeline for neoantigen
872 discovery to advance personalized cancer immunotherapy. *Nat Biotechnol*
873 (2024). https://doi.org/10.1038/s41587-024-02420-y
874 38 Goodman, A. M. *et al.* Tumor Mutational Burden as an Independent Predictor
875 of Response to Immunotherapy in Diverse Cancers. *Mol Cancer Ther* **16**, 2598-
876 2608 (2017). https://doi.org/10.1158/1535-7163.MCT-17-0386
877 39 Hellmann, M. D. *et al.* Nivolumab plus Ipilimumab in Lung Cancer with a High
878 Tumor Mutational Burden. *N Engl J Med* **378**, 2093-2104 (2018).
879 https://doi.org/10.1056/NEJMoa1801946
880 40 Marabelle, A. *et al.* Efficacy of Pembrolizumab in Patients With Noncolorectal
881 High Microsatellite Instability/Mismatch Repair-Deficient Cancer: Results
882 From the Phase II KEYNOTE-158 Study. *J Clin Oncol* **38**, 1-10 (2020).
883 https://doi.org/10.1200/JCO.19.02105
884 41 Samstein, R. M. *et al.* Tumor mutational load predicts survival after
885 immunotherapy across multiple cancer types. *Nat Genet* **51**, 202-206 (2019).
886 https://doi.org/10.1038/s41588-018-0312-8
887 42 Zhou, Y. *et al.* Nivolumab plus ipilimumab versus pembrolizumab as
888 chemotherapy-free, first-line treatment for PD-L1-positive non-small cell lung
889 cancer. *Clin Transl Med* **10**, 107-115 (2020). https://doi.org/10.1002/ctm2.14

890 43 Hodi, F. S. *et al.* Improved survival with ipilimumab in patients with metastatic
891 melanoma. *N Engl J Med* **363**, 711-723 (2010).
892 https://doi.org/10.1056/NEJMoa1003466
893 44 Borghaei, H. *et al.* Nivolumab versus Docetaxel in Advanced Nonsquamous
894 Non-Small-Cell Lung Cancer. *N Engl J Med* **373**, 1627-1639 (2015).
895 https://doi.org/10.1056/NEJMoa1507643
896 45 Liu, C. *et al.* KRAS-G12D mutation drives immune suppression and the
897 primary resistance of anti-PD-1/PD-L1 immunotherapy in non-small cell lung
898 cancer. *Cancer Commun (Lond)* **42**, 828-847 (2022).
899 https://doi.org/10.1002/cac2.12327
900 46 Platten, M. *et al.* A vaccine targeting mutant IDH1 in newly diagnosed glioma.
901 *Nature* **592**, 463-468 (2021). https://doi.org/10.1038/s41586-021-03363-z
902 47 Schumacher, T. *et al.* A vaccine targeting mutant IDH1 induces antitumour
903 immunity. *Nature* **512**, 324-327 (2014). https://doi.org/10.1038/nature13387
904 48 Hsiue, E. H. *et al.* Targeting a neoantigen derived from a common TP53
905 mutation. *Science* **371** (2021). https://doi.org/10.1126/science.abc8697
906 49 Hu, Z. *et al.* Personal neoantigen vaccines induce persistent memory T cell
907 responses and epitope spreading in patients with melanoma. *Nat Med* **27**, 515-
908 525 (2021). https://doi.org/10.1038/s41591-020-01206-4
909 50 Apoorvi, T., Yury, P., Iryna, V. & Michelle, K. Phosphopeptide Neoantigens as
910 Emerging Targets in Cancer Immunotherapy. *J Cancer Immunol (Wilmington)*
911 **6**, 135-147 (2024). https://doi.org/10.33696/cancerimmunol.6.094
912 51 Gubin, M. M. *et al.* Checkpoint blockade cancer immunotherapy targets
913 tumour-specific mutant antigens. *Nature* **515**, 577-581 (2014).
914 https://doi.org/10.1038/nature13988
915 52 McGranahan, N. *et al.* Clonal neoantigens elicit T cell immunoreactivity and
916 sensitivity to immune checkpoint blockade. *Science* **351**, 1463-1469 (2016).
917 https://doi.org/10.1126/science.aaf1490
918 53 Schumacher, T. N. & Schreiber, R. D. Neoantigens in cancer immunotherapy.
919 *Science* **348**, 69-74 (2015). https://doi.org/10.1126/science.aaa4971
920 54 Yadav, M. *et al.* Predicting immunogenic tumour mutations by combining mass
921 spectrometry and exome sequencing. *Nature* **515**, 572-576 (2014).
922 https://doi.org/10.1038/nature14001
923 55 Rosenberg, S. A. & Restifo, N. P. Adoptive cell transfer as personalized
924 immunotherapy for human cancer. *Science* **348**, 62-68 (2015).
925 https://doi.org/10.1126/science.aaa4967
926 56 Snyder, A. *et al.* Genetic basis for clinical response to CTLA-4 blockade in
927 melanoma. *N Engl J Med* **371**, 2189-2199 (2014).
928 https://doi.org/10.1056/NEJMoa1406498
929 57 Jackson, S. P. & Bartek, J. The DNA-damage response in human biology and
930 disease. *Nature* **461**, 1071-1078 (2009). https://doi.org/10.1038/nature08467
931 58 Brown, J. S., O'Carrigan, B., Jackson, S. P. & Yap, T. A. Targeting DNA Repair

932 in Cancer: Beyond PARP Inhibitors. *Cancer Discov* **7**, 20-37 (2017).
933 https://doi.org/10.1158/2159-8290.CD-16-0860
934 59 Olive, J. F. *et al.* Accounting for tumor heterogeneity when using CRISPR-Cas9
935 for cancer progression and drug sensitivity studies. *PLoS One* **13**, e0198790
936 (2018). https://doi.org/10.1371/journal.pone.0198790
937 60 Parsels, L. A. *et al.* Translation of DNA Damage Response Inhibitors as
938 Chemoradiation Sensitizers From the Laboratory to the Clinic. *Int J Radiat*
939 *Oncol Biol Phys* **111**, e38-e53 (2021).
940 https://doi.org/10.1016/j.ijrobp.2021.07.1708
941 61 Laumont, C. M. *et al.* Global proteogenomic analysis of human MHC class I-
942 associated peptides derived from non-canonical reading frames. *Nat Commun*
943 **7**, 10238 (2016). https://doi.org/10.1038/ncomms10238
944 62 Mohler, K. & Ibba, M. Translational fidelity and mistranslation in the cellular
945 response to stress. *Nat Microbiol* **2**, 17117 (2017).
946 https://doi.org/10.1038/nmicrobiol.2017.117
947 63 Laumont, C. M. *et al.* Noncoding regions are the main source of targetable
948 tumor-specific antigens. *Sci Transl Med* **10** (2018).
949 https://doi.org/10.1126/scitranslmed.aau5516
950 64 Chong, C. *et al.* Integrated proteogenomic deep sequencing and analytics
951 accurately identify non-canonical peptides in tumor immunopeptidomes. *Nat*
952 *Commun* **11**, 1293 (2020). https://doi.org/10.1038/s41467-020-14968-9
953 65 Ouspenskaia, T. *et al.* Unannotated proteins expand the MHC-I-restricted
954 immunopeptidome in cancer. *Nat Biotechnol* **40**, 209-217 (2022).
955 https://doi.org/10.1038/s41587-021-01021-3
956 66 Ruiz Cuevas, M. V. *et al.* Most non-canonical proteins uniquely populate the
957 proteome or immunopeptidome. *Cell Rep* **34**, 108815 (2021).
958 https://doi.org/10.1016/j.celrep.2021.108815
959 67 Weller, C. *et al.* Translation dysregulation in cancer as a source for targetable
960 antigens. *Cancer Cell* **43**, 823-840 e818 (2025).
961 https://doi.org/10.1016/j.ccell.2025.03.003
962 68 Kimura, S. & Suzuki, T. Fine-tuning of the ribosomal decoding center by
963 conserved methyl-modifications in the Escherichia coli 16S rRNA. *Nucleic*
964 *Acids Res* **38**, 1341-1352 (2010). https://doi.org/10.1093/nar/gkp1073
965 69 Baudin-Baillieu, A. *et al.* Nucleotide modifications in three functionally
966 important regions of the Saccharomyces cerevisiae ribosome affect translation
967 accuracy. *Nucleic Acids Res* **37**, 7665-7677 (2009).
968 https://doi.org/10.1093/nar/gkp816
969 70 Xing, M. *et al.* The 18S rRNA m(6) A methyltransferase METTL5 promotes
970 mouse embryonic stem cell differentiation. *EMBO Rep* **21**, e49863 (2020).
971 https://doi.org/10.15252/embr.201949863
972 71 Lin, M. *et al.* Targeting fibrinogen-like protein 1 enhances immunotherapy in
973 hepatocellular carcinoma. *J Clin Invest* **133** (2023).

https://doi.org/10.1172/JCI164528

72 Zhi, Y. *et al.* FBL promotes hepatocellular carcinoma tumorigenesis and progression by recruiting YY1 to enhance CAD gene expression. *Cell Death Dis* **16**, 348 (2025). https://doi.org/10.1038/s41419-025-07684-z

73 van Tran, N. *et al.* The human 18S rRNA m6A methyltransferase METTL5 is stabilized by TRMT112. *Nucleic Acids Res* **47**, 7719-7733 (2019). https://doi.org/10.1093/nar/gkz619

74 Golstein, P. & Griffiths, G. M. An early history of T cell-mediated cytotoxicity. *Nat Rev Immunol* **18**, 527-535 (2018). https://doi.org/10.1038/s41577-018-0009-3

75 Aktas, E., Kucuksezer, U. C., Bilgic, S., Erten, G. & Deniz, G. Relationship between CD107a expression and cytotoxic activity. *Cell Immunol* **254**, 149-154 (2009). https://doi.org/10.1016/j.cellimm.2008.08.007

76 Rong, B. *et al.* Ribosome 18S m(6)A Methyltransferase METTL5 Promotes Translation Initiation and Breast Cancer Cell Growth. *Cell Rep* **33**, 108544 (2020). https://doi.org/10.1016/j.celrep.2020.108544

77 Li, X., Yang, G., Ma, L., Tang, B. & Tao, T. N(6)-methyladenosine (m(6)A) writer METTL5 represses the ferroptosis and antitumor immunity of gastric cancer. *Cell Death Discov* **10**, 402 (2024). https://doi.org/10.1038/s41420-024-02166-1

78 Langmead, B., Trapnell, C., Pop, M. & Salzberg, S. L. Ultrafast and memory-efficient alignment of short DNA sequences to the human genome. *Genome Biol* **10**, R25 (2009). https://doi.org/10.1186/gb-2009-10-3-r25

79 Dobin, A. *et al.* STAR: ultrafast universal RNA-seq aligner. *Bioinformatics* **29**, 15-21 (2013). https://doi.org/10.1093/bioinformatics/bts635

80 Pertea, M. *et al.* StringTie enables improved reconstruction of a transcriptome from RNA-seq reads. *Nat Biotechnol* **33**, 290-295 (2015). https://doi.org/10.1038/nbt.3122

81 Zhong, Y. *et al.* RiboDiff: detecting changes of mRNA translation efficiency from ribosome footprints. *Bioinformatics* **33**, 139-141 (2017). https://doi.org/10.1093/bioinformatics/btw585

82 Xiao, Z. *et al.* De novo annotation and characterization of the translatome with ribosome profiling data. *Nucleic Acids Res* **46**, e61 (2018). https://doi.org/10.1093/nar/gky179

83 Lu, T. *et al.* Deep learning-based prediction of the T cell receptor-antigen binding specificity. *Nat Mach Intell* **3**, 864-875 (2021). https://doi.org/10.1038/s42256-021-00383-2

1013 **FIGURE LEGENDS**

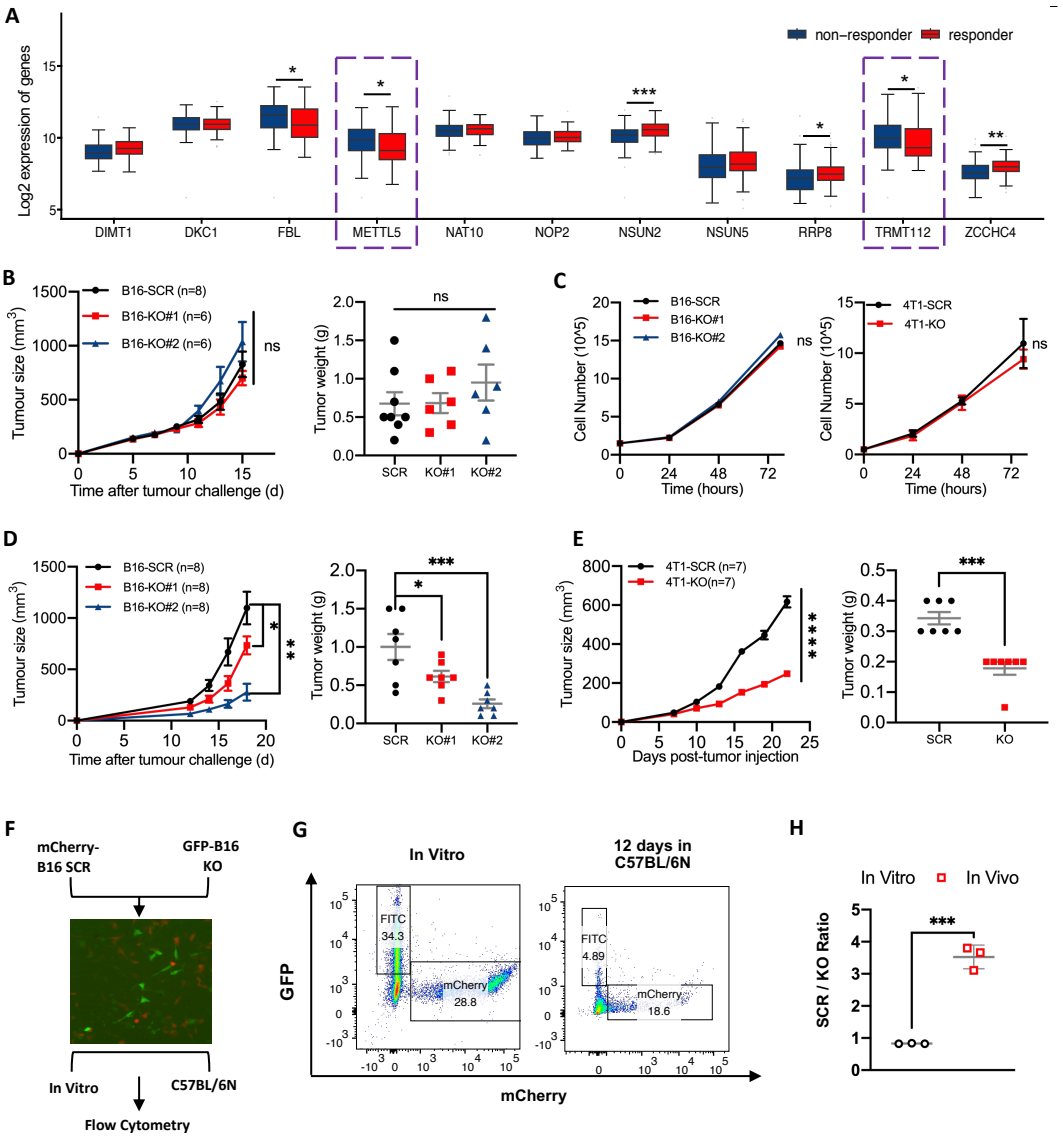

1014

1015 **Fig. 1: METTL5 depletion attenuates tumour growth**

1016 **A**, Relationship between the expression levels of certain RNA modification enzymes

1017 and response to immune checkpoint blockade (ICB) therapy. METTL5 and TRMT112

1018 are highlighted with purple boxes.

1019 **B**, Growth curve of tumors in nude mice subcutaneously implanted with B16-F10 SCR

1020 or METTL5 deficiency cells. The tumor growth (left) and final tumor weights (right)

1021 were compared.

1022 **C**, In vitro proliferation assay of SCR and Mettl5-KO cells in B16-F10 (left) and 4T1

1023 (right) cell lines.

1024 **D**, Growth curve of tumors in C57BL/6N mice subcutaneously implanted with B16-
1025 F10 SCR or Mettl5-KO cells. The tumor growth (left) and final tumor weights (right)
1026 were compared.
1027 **E**, Growth curve of tumors in Balb/c mice subcutaneously implanted with 4T1 SCR or
1028 Mettl5-KO cells. The tumor growth (left) and final tumor weights (right) were
1029 compared.
1030 **F-H**, In vivo competition assay between mCherry-labeled SCR control and GFP-
1031 labeled Mettl5-KO B16-F10 cells. Schematic diagram of the competitive growth assay
1032 (**F**). mCherry-labeled SCR and GFP-labeled-KO cells were mixed at a 1:1 ratio and
1033 either subcutaneously injected into C57BL/6N mice or co-cultured in vitro. Cell ratios
1034 were quantified by flow cytometry on Day 12. Representative flow cytometry plots
1035 showing the composition of SCR and Mettl5-KO cells (**G**). Quantitative analysis of cell
1036 population ratios (**H**).
1037 **Note: A**, Data from The Cancer Genome Atlas (TCGA) and were presented as median
1038 (IQR 25-75%, n=154). Student's t-tests. **B**, **D**, two-way ANOVA (left) and One-way
1039 ANOVA with Tukey's test (right). **C**, two-way ANOVA. **E**, two-way ANOVA (left)
1040 and Student's t-tests (right). **H**, Student's t-tests. **B**, **D**, **E**, Data were presented as mean
1041 ± SEM. **C**, **H**, Data were represented as mean ± SD (n=3). *P<0.05, **P<0.01,
1042 ***P<0.001, ns: not significant.
1043

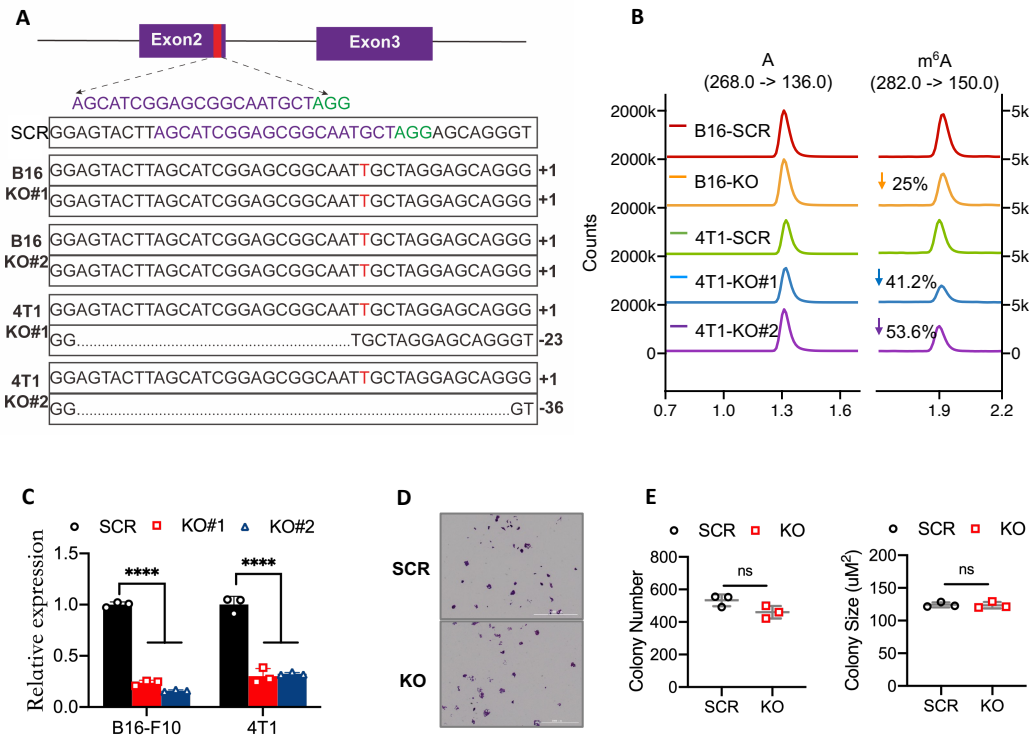

sFig. 1: Genetic ablation of METTL5 via CRISPR-Cas9 and its effect on tumour-cell growth in vitro

A, Schematic diagram of sgRNA targeting mouse *Mettl5* locus. Sanger sequencing was used to confirm CRISPR-Cas9-mediated knockout.

B, HPLC-MS/MS analysis of m^6A/A levels in total RNA purified from the SCR and METTL5 KO cells.

C, Knockout of *Mettl5* in B16-F10 cells and 4T1 cells were verified by Real-time quantitative PCR analysis.

D, **E**, Colony-formation assay of WT and METTL5 KO B16-F10 cells. 500 cells were seeded in a 6-well plate and cultured for six days, representative pictures (**D**) were taken, and the colony numbers and sizes (**E**) were measured.

Note: C, One-way ANOVA with Tukey's test. **E**, Student's t-tests (right). **C**, **E**, Data were represented as mean ± SD (n=3). ****P<0.0001, ns: not significant.

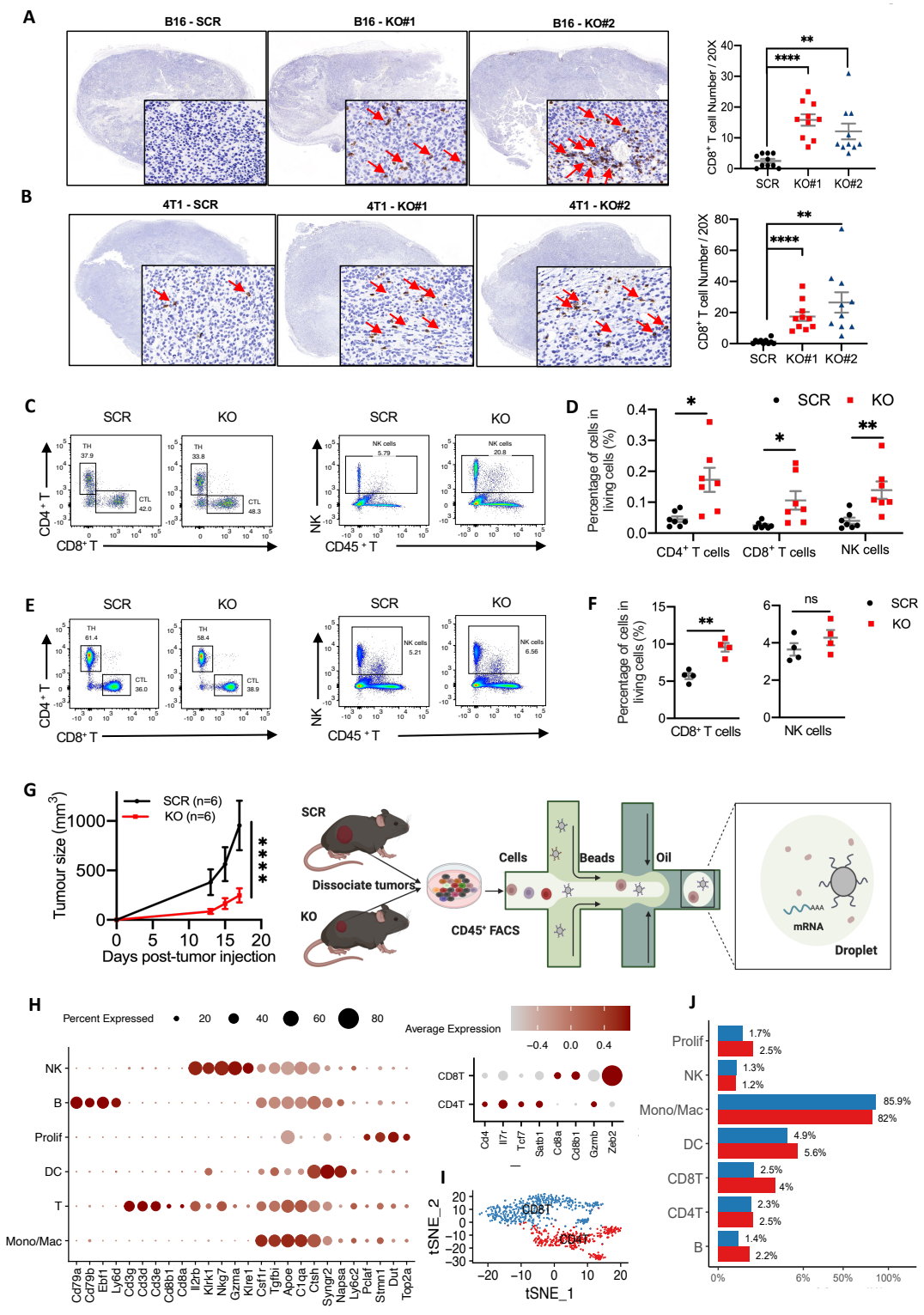

Fig. 2: METTL5 deficiency enhances tumor immune cell infiltration

A, **B**, Immunohistochemistry (IHC) detected CD8α⁺ cells in Mettl5-KO tumor tissues derived from B16-F10 (**A**) and 4T1 (**B**) models. Representative images (left) and

1063 quantified CD8α$^+$ cell counts (right) are shown. 10 random 20× fields per sample were
1064 analyzed. CD8α$^+$ cells are indicated by red arrows.
1065 **C-F**, Flow cytometry analysis of immune cell populations in the tumor
1066 microenvironment (**C**) and spleen (**E**) of C57BL/6N mice inoculated with SCR or
1067 Mettl5-KO B16-F10 cells, and representative flow cytometry image showing the
1068 distribution of CD4$^+$ T cells, CD8$^+$ T cells (left) and NK cells(right). The relative
1069 frequency of immune cells amongst living cells from tumors (**D**) and spleen (**F**) were
1070 assessed.
1071 **G**, Workflow schematic of single-cell sequencing for tumor tissues. In vivo tumor
1072 growth kinetics in C57BL/6 mice inoculated with SCR or Mettl5-KO B16-F10 cells.
1073 Tumors were excised and dissociated at days 18 post-inoculation, followed by CD45$^+$
1074 immune cell enrichment and single-cell sequencing.
1075 **H**, Dot plot illustrates the clustering analysis results of single-cell sequencing data (left).
1076 T cells were isolated from the total immune cell population and further stratified into
1077 CD8$^+$ T cells and CD4$^+$ T cell subsets (right). Dot color indicates expression level and
1078 dot size indicates the proportion of each cell type expressing each gene.
1079 **I**, t-SNE plots show T-cell subpopulations derived from tumors, including CD4$^+$ T-cell
1080 and CD8$^+$ T-cell subpopulations.
1081 **J**, Bar chart shows the proportion of tumor - infiltrating immune cell populations, with
1082 blue representing the METTL5- knockout group and red the control group.
1083 **Note: A**, **B**, One-way ANOVA with Tukey's test. **D**, **F**, Student's t-tests (right). **A**, **B**,
1084 **D**, **F**, Data were represented as mean ± SD. *P<0.05, **P<0.01, ****P<0.0001, ns: not
1085 significant.
1086

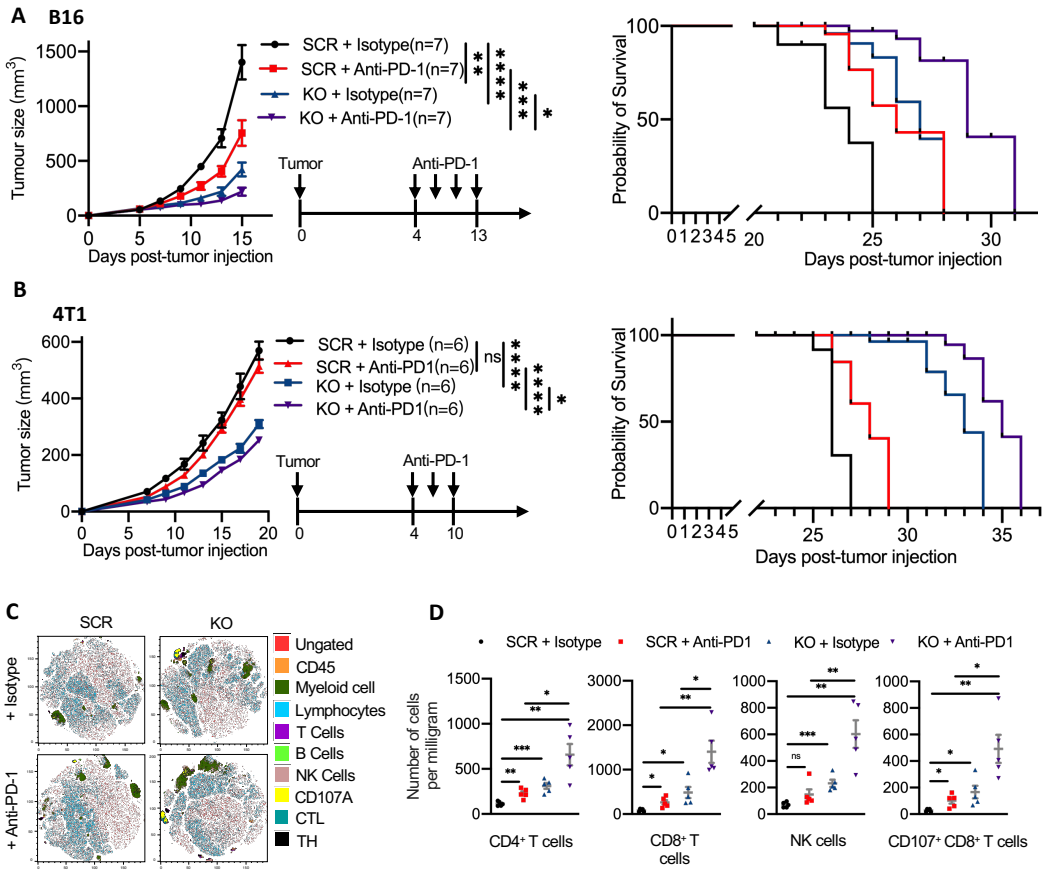

Fig. 3: Inhibition of Mettl5 increases the efficacy of tumor immunotherapy

A, Anti-PD-1 antibody was administered to Mettl5-KO and SCR B16-F10 tumor-bearing C57BL/6N mice on days 4, 7, 10, and 13 post-implantation, followed by longitudinal monitoring of tumor volume (left) and overall survival (right).

B, Anti-PD-1 antibody was administered to Mettl5-KO and SCR B16-F10 tumor-bearing Balb/c mice on days 4, 7, and 10 post-implantation, followed by longitudinal monitoring of tumor volume (left) and overall survival (right).

C, t-SNE analysis of immune cell populations in the tumor microenvironment of tumor in C57BL/6N mice. Mice were treated with either isotype control or anti-PD-1 antibody. The analysis includes the following immune cell populations: Lymphocytes, $CD45^+$ cells, Myeloid cells, T Cells, B Cells, NK Cells, $CD107a^+$ cells, CTL, and T Helper (TH) cells. The plots show the distribution of these immune cell populations in the tumor microenvironment for SCR and KO groups treated with isotype control or anti-PD-1 antibody.

1102 **D**, Quantitative analysis of immune cell populations in the tumor microenvironment of
1103 tumor in C57BL/6N mice. The number of $CD4^+$ T cells, $CD8^+$ T cells, NK cells, and
1104 CD107 a + $CD8^+$ T cells per milligram of tumor tissue was determined by flow
1105 cytometry.
1106 **Note:** Mouse survival curves were plotted using endpoints: death or tumor volume
1107 exceeding 2000 mm^3. **A**, **B**, two-way ANOVA. Data were presented as mean ± SEM.
1108 **D**, Student's t-tests. Data were represented as mean ± SD (n=5). *P<0.05, **P<0.01,
1109 ***P<0.001, ****P<0.0001, ns: not significant.

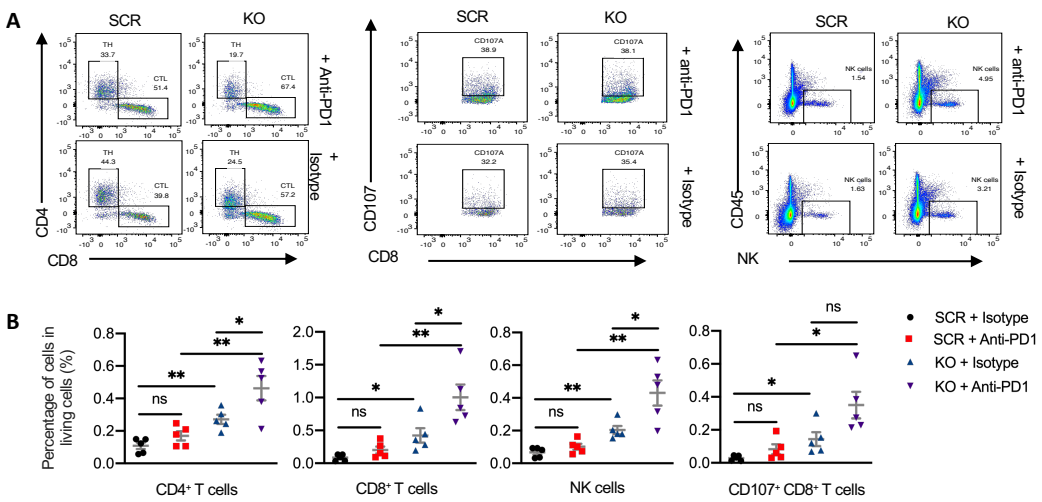

1110

1111 **sFig. 3: Depletion of PTRHD1 enhances intra-tumoral T-cell infiltration**

1112 **A**, **B**, Representative flow cytometry image (**A**) showing the distribution of $CD4^+$ T

1113 cells, $CD8^+$ T cells (left), CD107a+ $CD8^+$ T cells (middle), and NK cells(right). The

1114 relative frequency of immune cells amongst living cells (**B**) were assessed.

1115 **Note: B**, Student's t-tests. Data were represented as mean ± SD (n=5). **P*<0.05,

1116 ***P*<0.01, ns: not significant.

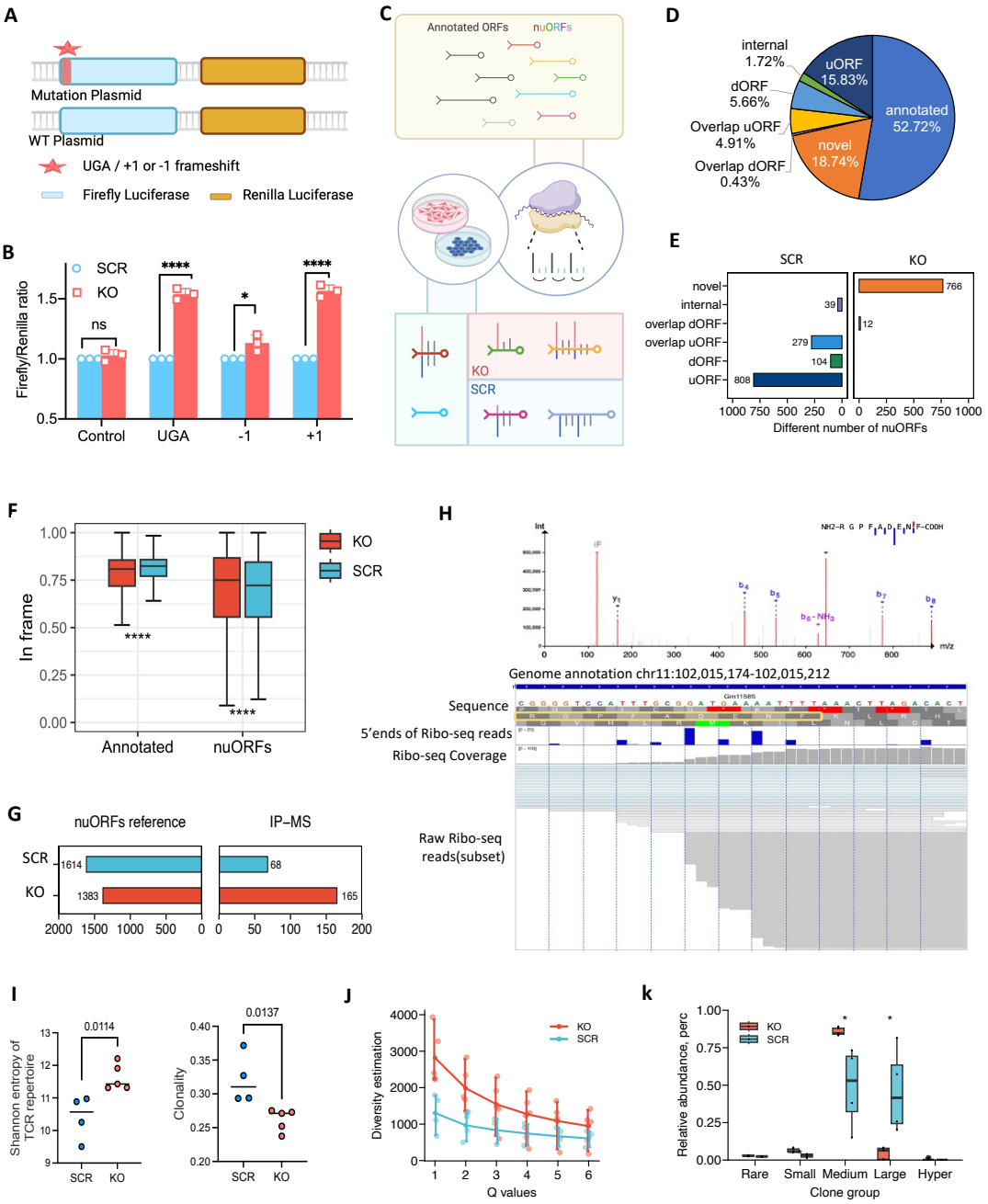

Fig. 4: Depletion of METTL5 induces neoantigen generation

A, Scheme of reporter vector. Dual-luciferase plasmid constructs were designed with a UGA stop codon, +1 frameshift, or -1 frameshift upstream of the firefly luciferase gene, with Renilla luciferase as an internal control.

B, Translation efficiency of firefly luciferase in SCR and METTL5 KO cells was revealed by a reporter assay. Firefly luciferase activity was normalized to Renilla luciferase, with the SCR group set as the baseline (relative ratio = 1).

1125 **C**, Workflow schematic of nuORFdb v.1.0 generation. ORFs from ribosome profiling
1126 (Ribo-seq) data were classified into annotated ORFs and novel ORFs (nuORFs), which
1127 were compiled as a database for subsequent analyses. For differential nuORF
1128 expression between Mettl5-KO and SCR groups, we classified nuORFs into three
1129 categories: (1) Shared nuORFs (expressed in both groups with <1.5-fold TPM
1130 difference), (2) Mettl5-KO -specific nuORFs (exclusive to Mettl5-KO or with ≥1.5-
1131 fold higher TPM than SCR), and (3) SCR-specific nuORFs (exclusive to SCR or with
1132 ≥1.5-fold higher TPM than Mettl5-KO).
1133 **D**, Pie chart illustrating the classification of nuORFs identified in Mettl5-KO and SCR
1134 group. The chart shows the percentage distribution of different nuORF categories
1135 relative to the total nuORFs.
1136 **E**, Differential analysis of nuORF categories between Mettl5-KO and SCR groups.
1137 **F**, Distribution of in-frame translation events in Mettl5-KO and SCR groups across
1138 annotated ORFs and nuORFs.
1139 **G**, Peptides eluted from MHC-I immunoprecipitates in SCR and Mettl5-KO samples
1140 were identified using corresponding nuORFs (>8 aa) as reference sequences.
1141 **H**, A representative nuORF-derived peptide NH2-R-G-F-P-A-D-N-F-COOH) in
1142 Mettl5-KO tumors. The characteristic 3-nucleotide periodicity of ribosome-protected
1143 fragments confirmed its translational activity.
1144 **I**, Scatter plots depict comparative distributions of TCR repertoire diversity (Shannon
1145 entropy) and clonality between Mettl5-KO and SCR groups.
1146 **I**, Comparative diversity analysis (Hill numbers q=1–6) between Mettl5-KO and SCR
1147 groups.
1148 **J**, Violin plots showing the distribution of clonal expansion levels in Mettl5-KO versus
1149 SCR groups, with clones categorized by abundance thresholds: Rare (<1e-05), Small
1150 (1e-04), Medium (0.001), Large (0.01), and Hyperexpanded (1).

1151 **Note: B**, **F**, **I, K**, Student's t-tests. **B**, **I,** Data were represented as mean ± SD. **F**, **K**,
1152 Data were presented as median (IQR 25-75%). *P<0.05, ****P<0.0001, ns: not
1153 significant.

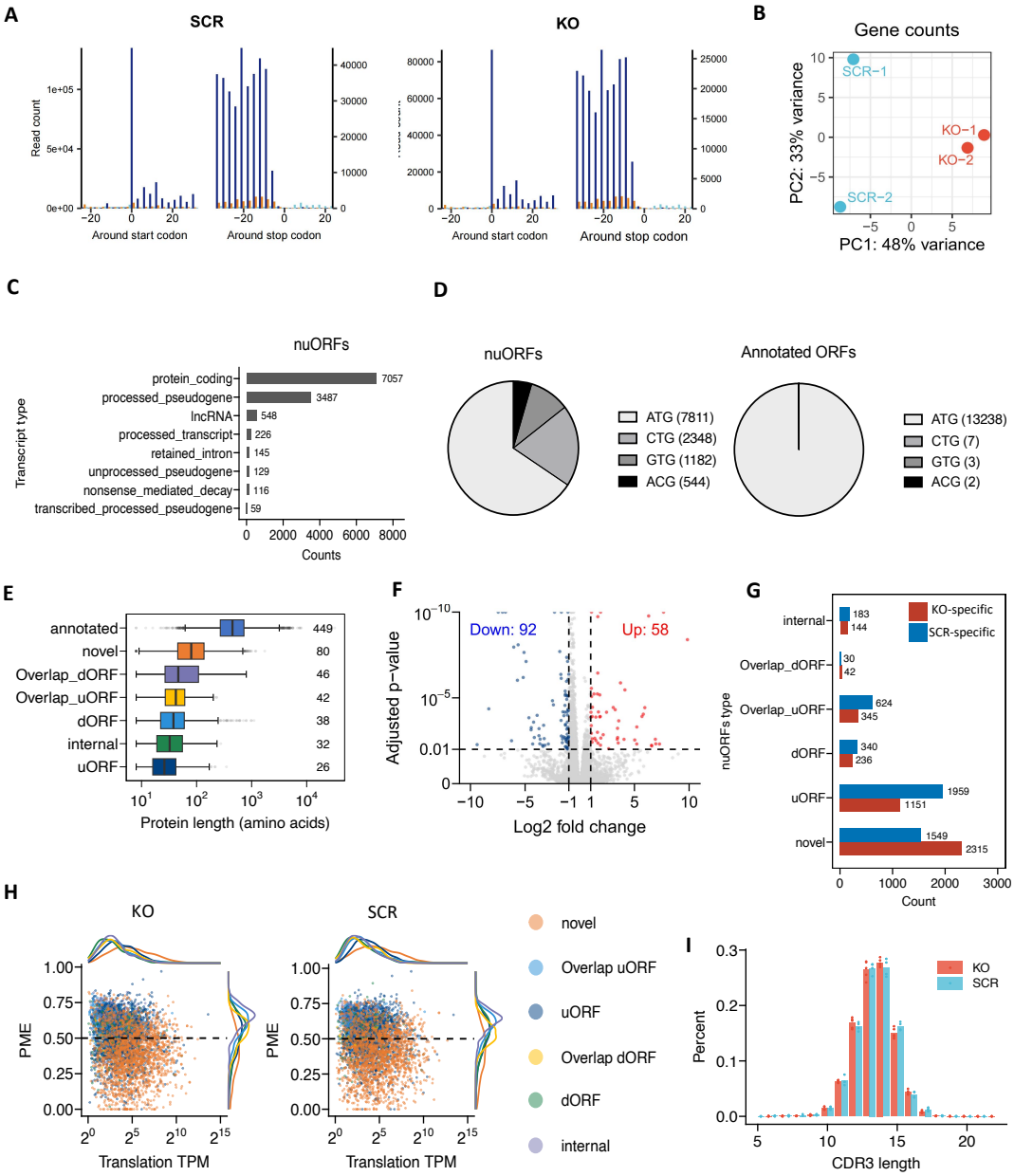

sFig. 4: Identification of novel ORFs induced by METTL5 deficiency

A, Quality control of Ribo-seq data in SCR (left) and METTL5 KO (right) cells.

B, The PCA plot shows the separation between Mettl5-KO and SCR groups based on gene counts

C, Distribution of transcript types for nuORFs identified by Ribo-seq.

D, Distribution of start codons for nuORFs and annotated ORFs in Mettl5-KO and SCR groups.

1162 **E**, Protein length distribution (in amino acids) for different ORF categories in Mettl5-
1163 KO and SCR groups.
1164 **F**, Volcano plot depicting down-regulated (blue) and up-regulated (red) genes
1165 identified by Ribo-seq in METTL5 KO cells compared with SCR cells.
1166 **G**, Differential counts of nuORF types between Mettl5-KO and SCR groups. Red bars
1167 indicate KO-specific nuORFs (present only in the KO group or with a TPM exceeding
1168 that in the SCR group by 1.5-fold), while blue bars indicate SCR-specific nuORFs
1169 (present only in the SCR group or with a TPM exceeding that in the KO group by 1.5-
1170 fold).
1171 **H**, Translation activity analysis of different ORF categories in Mettl5-KO and SCR
1172 groups. Higher PME values indicate more active translation. The dashed line at PME =
1173 0.5 represents a threshold for translation efficiency.
1174 **I**, Scatter plot from TCR-seq quality control showing no significant differences in
1175 CDR3 length distribution between KO and SCR groups.
1176

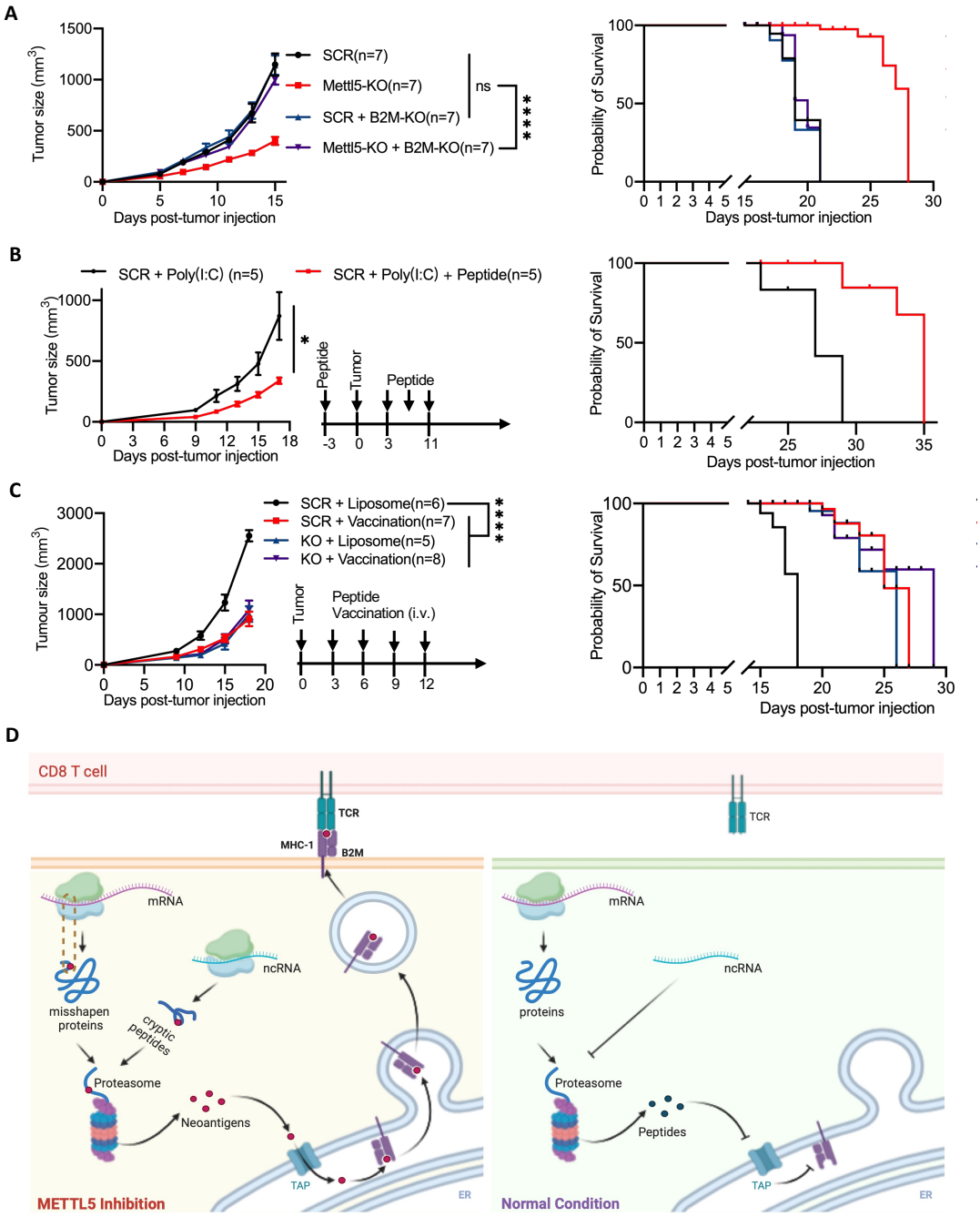

Fig. 5: Combination of neoantigen vaccination and METTL5 inhibition elicits robust antitumour immune response

A, Growth curve of tumors in C57BL/6N mice subcutaneously implanted with SCR, Mettl5-KO, SCR plus B2M-KO, Mettl5-KO plus B2M-KO B16-F10 cells. The tumor growth (left) and overall survival (right) were compared.

1183 **B**, C57BL/6 mice bearing B16-F10 tumor were immunized with selected neoantigen-
1184 encoded peptides or the adjuvant poly(I:C) on days -3, 3, 7, and 11. The tumor growth
1185 (left) and overall survival (right) were compared.
1186 **C**, C57BL/6 mice subcutaneously implanted with SCR or Mettl5-KO B16-F10 cells
1187 were immunized with the neoantigen mRNA vaccination and liposome on days 3, 6, 9,
1188 and 12. The tumor growth (left) and overall survival (right) were compared.
1189 **D**, Working model for the critical role of METTL5 in tumor immunity through
1190 neoantigen generation. METTL5 deficiency abrogates m^6A deposition in the ribosomal
1191 decoding center, impairing ribosomal function and compromising translation fidelity.
1192 These defects lead to aberrant non-canonical translation events that generate
1193 immunogenic neoantigens, thereby stimulating anti-tumor immunity.
1194 **Note:** Mouse survival curves were plotted using endpoints: death or tumor volume
1195 exceeding 2000 mm^3. **A**, **B**, **C**, Student's t-tests. Data were presented as mean ± SEM.
1196 *P<0.05, ****P<0.0001, ns: not significant.
1197

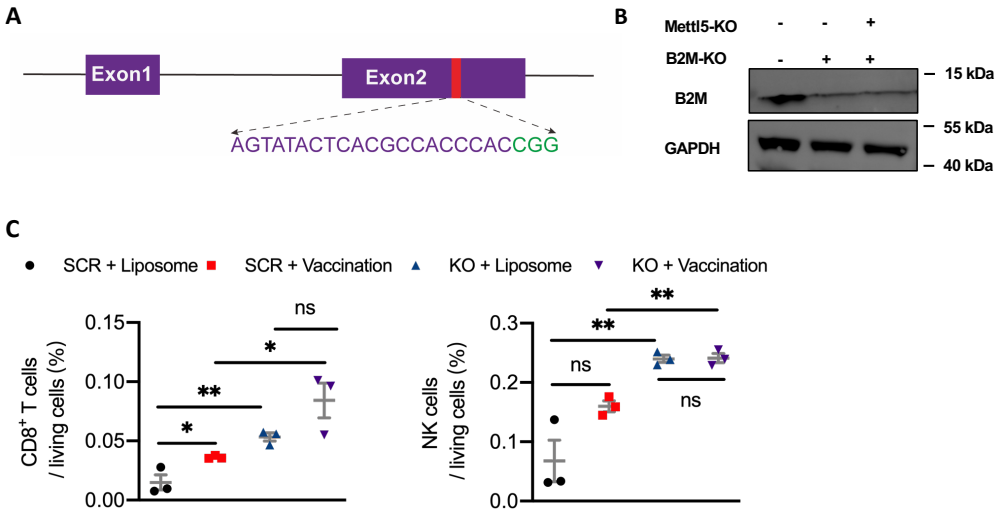

sFig. 5: Generation of B2M knockout cell lines

A, Schematic diagram of sgRNA targeting mouse *B2M* locus.

B, Western blotting confirmed the depletion of B2M in SCR and Mettl5-KO B16-F10 cells. GAPDH was used as internal control.

C, Flow cytometry analysis of immune cell infiltration in tumors of C57BL/6N mice bearing SCR or Mettl5-KO B16-F10 cells following neoantigen mRNA-liposome vaccination. The frequencies of CD4+ T cells and CD8+ T cells were quantified within live cell populations.

Note: C, Student's t-tests. Data were presented as mean ± SD. *P<0.05, **P<0.01, ns: not significant.